Fall 2020

An EMI characterization and modeling study for consumer electronics and integrated circuits

Chunyu Wu

Department: Electrical and Computer Engineering

AN EMI CHARACTERIZATION AND MODELING STUDY FOR CONSUMER ELECTRONICS AND INTEGRATED CIRCUITS

by

CHUNYU WU

A DISSERTATION

Presented to the Graduate Faculty of the

MISSOURI UNIVERSITY OF SCIENCE AND TECHNOLOGY

In Partial Fulfillment of the Requirements for the Degree

DOCTOR OF PHILOSOPHY

in

ELECTRICAL ENGINEERING

2020

Approved by:

Jun Fan, Advisor
Daryl G. Beetner
Mehdi Ferdowsi
Victor Khilkevich
Yanjie Fu

PUBLICATION DISSERTATION OPTION

This dissertation consists of the following three papers, formatted in the style used by the Missouri University of Science and Technology:

Paper I, found on pages 3–28, has been submitted to *IEEE Transactions on Electromagnetic Compatibility*.

Paper II, found on pages 29–55, has been published in *IEEE Transactions on Electromagnetic Compatibility*, vol. 61, no. 6, pp. 2050-2059, Dec. 2019.

Paper III, found on pages 56–78, is intended for submission to *IEEE Transactions on Electromagnetic Compatibility*.

ABSTRACT

As internet-of-things (IoT) applications surge, wireless connectivity becomes an essential part of the network. Smart home, one of the most promising application scenarios of IoT, will improve our life quality enormously. However, electromagnetic interference (EMI) to the receiving antenna, either from another electronic product or from a module/an integrated circuit(IC) inside the same wireless device, will degrade the performance of wireless connectivity, thus influencing the user experience. Characterization and modeling of the EMI become increasingly important.

In the first part, an improved method to extract equivalent dipoles from magnitude-only electromagnetic-field data based on the genetic algorithm and back-and-forth iteration algorithm is proposed. The method provides an automatic flow to extract the equivalent dipoles from electromagnetic-field data on arbitrarily shaped scanning surfaces and minimizes the number of extracted dipoles. In the second part, both the differential mode (DM) and common mode (CM) EMI below 1 MHz from the ac-dc power supply in a LED TV is analyzed and modeled. Through joint time-frequency analysis, the drain-to-source voltage of the power MOSFET in the power factor correction (PFC) converter is identified as the dominant noise source of both CM and DM EMI below 1 MHz from the power supply. The current paths of DM and CM EMI are explained and modeled by a linear equivalent circuit model. In the last part, the noise source and current path of the conducted CM EMI noise from a Qi-compliant wireless power transfer (WPT) system for mobile applications are analyzed. The analysis and modeling explain the mechanism of the CM EMI noise and provide guidelines to reduce the CM EMI noise.

ACKNOWLEDGMENTS

First and foremost, I would like to express my sincere gratitude to my advisor, Prof. Jun Fan, for his continuous support during my Ph.D. study, and for his patience, motivation, and guidance. His guidance helped me tremendously in finding the research direction and career path.

Besides my advisor, I would like to thank the rest of my dissertation committee: Prof. Daryl Beetner, Prof. Mehdi Ferdowsi, Prof. Victor Khilkevich, and Prof. Yanjie Fu, for their insightful comments and encouragement.

My sincere thanks also goes to the whole EMC group, other professors who taught me courses, and staff who helped me at Missouri S&T. The past six years in the EMC group has been a wonderful memory in my life.

Last but not least, I would like to thank my family for supporting me mentally throughout my life.

TABLE OF CONTENTS

SECTION

LIST OF ILLUSTRATIONS

PAPER I Page

PAPER II

LIST OF TABLES

PAPER I Page

1. INTRODUCTION

1.1. BACKGROUND

EMI is a disturbance generated by a noise source that affects an electrical circuit by radiation or conduction. The disturbance may degrade the performance of the circuit or even stop it from functioning. Any device that has electronic circuitry can be susceptible to EMI. With the ever-increasing use of the electromagnetic spectrum and the more sophisticated electronic equipment, issues of EMI are attracting attention.

When addressing EMI issues, consider a noise source, a path, and a victim. The noise from the source propagates through the path and interferes with the operation of the victim. All three must exist to have an EMI problem.

Based on the location of the noise source, EMI issues can be divided into two categories. In the first category, the noise source is in a different electronic equipment. The emissions from electronic equipment are regulated by EMC standards known as radiated emission limits and conducted emission limits. In the second category, the noise source and victim are in the same electronic equipment. Specifically, if the victim is a wireless receiver, EMI issues can cause RF de-sense problems.

Based on the type of coupling path, EMI issues can be divided into two categories: conducted EMI and radiated EMI. In conducted EMI, the noise propagates through electrical currents with a direct electrical contact, for example, the power line and data line. In radiated EMI, the noise propagates through electromagnetic fields without direct electrical contact, for example, near-field coupling and far-field radiation.

EMI Modeling is complicated and difficult due to several reasons. First, EMI is often caused by parasitic elements (capacitances or inductances) which are often neglected and difficult to characterize. Second, EMI is related to not only the electrical design, but also the mechanical design of electronic equipment, for example, the shielding can, the cable braid, and the metal chassis, thus EMI modeling relies on accurate modeling of the whole system and incorporates both circuit simulation and full-wave simulation. Last but not least, the schematic or layout information of ICs, components, and modules are often not available from the vendor.

There are generally two different EMI modeling methods. The first modeling method is physics-based, which demonstrates the flow of the EMI current and explains the EMI mechanism. The second modeling method is black-box modeling, which does not require knowledge of the EMI mechanism. The physics-based model is usually more complicated than the black-box model.

1.2. CONTENTS

This dissertation consists of three papers. The first paper is related to the modeling of radiated EMI using the black-box modeling method. The second and third papers are related to the modeling of conducted EMI using the physics-based modeling method.

PAPER

I. A HYBRID ALGORITHM OF GENETIC ALGORITHM AND IMPROVED ITERATION ALGORITHM FOR EXTRACTION OF EQUIVALENT DIPOLES FROM MAGNITUDE-ONLY ELECTROMAGNETIC FIELDS

Chunyu Wu, Ze Sun, Xu Wang, Yansheng Wang, Ben Kim, and Jun Fan

ABSTRACT

Infinitesimal electric and magnetic dipoles are widely used as an equivalent radiating source model. In this paper, an improved method to extract equivalent dipoles from magnitude-only electromagnetic-field data based on the genetic algorithm and back-and-forth iteration algorithm is proposed. The method provides an automatic flow to extract the equivalent dipoles without a prior decision of the number, type, and position of dipoles and minimizes the number of extracted dipoles. The extracted dipoles can be close to the current flow of the original radiating source. Compared with the conventional back-and-forth iteration algorithm, it can be applied to electromagnetic-field data on a single scanning surface with arbitrary shape. Compared to the conventional genetic algorithm-based method, this method reduces the optimization time and converges at a lower relative error. This method is validated by both simulation data, and measurement data and its advantages are proved.

1. INTRODUCTION

Infinitesimal dipoles are widely used as an equivalent model of radiating source in far-field radiated emissions, near-field coupling, and antenna modeling areas [1]. The infinitesimal dipoles which generate the same radiated electromagnetic fields can be used to replace the original radiating noise source.

These equivalent dipoles can be directly applied to calculation of the far-field value as shown in [1][2] since radiation from infinitesimal dipoles is well known. This implies the application of equivalent dipoles in near-field to far-field transformation. They can also be imported in a full-wave simulation tool to simulate the far-field value of noise source with added enclosure [3] or near-field coupling from a noise source to a victim antenna [4]. In [5], a physics-based dipole is extracted and used to debug the radiation mechanism of a flexible printed circuit board (PCB). Physics-based dipoles that are close to the current flow of the original radiating source are useful in terms of finding the noise current path. However, the physics-based dipoles are extracted by recognizing the pattern generated by a single horizontal magnetic dipole. In other cases, the pattern may be complicated and cannot be recognized easily. Later, a dipole-based reciprocity method is proposed to calculate the coupled noise from a physics-based dipole to the victim antenna [6][7][8]. The direction and location of the physics-based dipole can be optimized to reduce the coupled noise. This can provide a guideline to optimize the placement of a noise source [9][10]. In conclusion, physics-based dipoles turn out to be useful in debugging radiation mechanisms (current flow), near-field coupling estimation, and its reduction. In [11], equivalent dipoles are used to correct the antenna pattern obtained off-center.

There are several methods to extract equivalent dipoles from the scanned electromagnetic fields. These methods can be divided into two categories.

The first category requires both the magnitude and phase of electromagnetic-field data. In [12], a set of vertical magnetic dipoles or horizontal electric dipoles are placed on the discretized horizontal surface of a radiating integrated circuit (IC) and linear least squares is used to solve the current intensity of these dipoles. The method requires simple matrix operations to obtain the results and is fast; however, the number of dipoles is large, and the location of dipoles needs to be determined in advance by meshing the surface of the IC. In [13], an array of uniformly placed dipole sets is used and each dipole set includes one vertical electric dipole *Pz* and two horizontal magnetic dipoles *Mx*, *My* at the same position. The regularization technique and truncated singular-value decomposition method are investigated with the conventional linear least squares to calculate the dipole magnitude and phase from the near-field data. By combining the genetic algorithm and linear least squares, equivalent dipoles are obtained with a reduced number of dipoles without a prior decision of the location and number of dipoles in [14]. There are mainly two differences between [14] and this paper. The first difference is that [14] requires both the magnitude and phase of electromagnetic fields, and the second difference is that [14] does not optimize the dipole type. It is assumed that only magnetic dipoles exist. In [15], a similar method to [14], adding optimization of dipole type, is applied in RF de-sense scenarios to model the radiation from an IC. In [16], a new equivalent dipole model hybrid with artificial neural network (ANN) is proposed to estimate near fields under a complex environment where free space or half-space Green's function does not apply.

Since accurate measurement of the phase of electromagnetic fields may not be available due to equipment cost and measurement reliability, especially at high frequencies, the second category of methods which requires only the magnitude of electromagnetic-field data is in demand. In [2], the genetic algorithm is used to optimize the type (electric or magnetic), position, orientation, magnitude, and phase of all dipoles. This method works well but the disadvantages are that the converged relative error is large and it is time-consuming, due to a large number of optimization variables (eight variables for each dipole) and the large optimization range of dipole magnitude which is from zero to positive infinity. Zhang and Fan propose a back-and-forth iteration algorithm that requires only the magnitude of electromagnetic fields on two near-field scanning planes to extract the dipoles [17]. This method originates from the Gerchberg-Saxton algorithm [18] and performs Fourier transform on the plane whose phase is known to obtain phase distribution on the other plane. This method is effective and fast at extracting dipoles from magnitude-only near-field data, but there are two disadvantages in this method. The first disadvantage is that the method requires propagating fields from the lower plane to the higher plane. This will bring some difficulties when cylindrical scanning or spherical scanning is used. The transformation between fields on two different cylindrical surfaces or spherical surfaces is more complicated than the transformation between fields on two different planar surfaces. The second disadvantage is that the dipole sets which include one vertical electric dipole *Pz* and two horizontal magnetic dipoles *Mx*, *My* at the same position are placed uniformly. This leads to a large number of dipoles and more scanning points to have a well-conditioned transformation matrix during the transformation from fields to dipole value. Also, the number and position of dipole sets need to be determined in advance. This is

usually done by trial and error. In [19], machine learning is used to recognize the near-field pattern as an image to extract dipoles. But the usefulness of the method is limited because it cannot work for near-field patterns which are not included in the training set.

In this paper, an improved method for dipole extraction from magnitude-only electromagnetic-field data based on the genetic algorithm and back-and-forth iteration algorithm is proposed, which aims at overcoming the disadvantages of previous methods mentioned above. The proposed method provides an automatic flow to extract the equivalent dipoles without a prior decision of the number, type, and position of dipoles and minimizes the number of extracted dipoles. It can also generate physics-based dipoles, which are close to the current flow of the original radiating source. Compared to the conventional back-and-forth iteration algorithm, this method can be applied to electromagnetic-field data on a single scanning surface with arbitrary shape. Compared with the conventional genetic algorithm-based method, this method reduces the optimization time and converges at a lower relative error because it will not optimize the magnitude and phase of the dipoles.

This paper is organized as follows. Section 2 introduces the method in detail. Section 3 validates the method using both simulation data and measurement data. Section 4 concludes the paper.

2. DESCRIPTION OF THE METHOD

The input data of the method can be either magnitude-only electric fields, magnetic fields, or both on arbitrarily shaped surfaces. In this section, magnitude-only electric fields

on cylindrical surfaces are taken as an example to describe the method. The principle of this method is shown in Figure 1. Electric fields with only magnitude are obtained first on two cylindrical surfaces around the DUT, then infinitesimal dipoles are extracted to generate the same electric fields. These infinitesimal dipoles are considered as an equivalent model of radiating source.

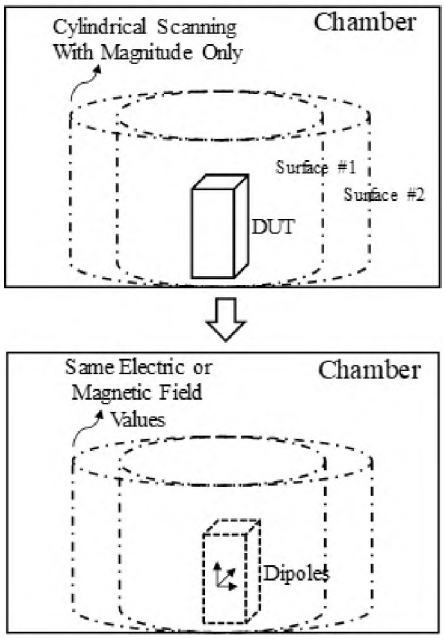

Figure 1. Principle of the method.

The general flow of this method is shown in Figure 2. The method starts with one dipole. Then, the genetic algorithm is used to optimize the dipole type and dipole position to minimize the relative error between the measured electric fields and the calculated electric fields from equivalent dipoles. The optimization process will be explained in Section 2.1. During optimization, the magnitude and phase of equivalent dipoles are determined from improved back-and-forth iteration which will be explained in Section 2.2.

After optimization, the minimized relative error will be compared with the previous relative error with one less dipole. If the decrease of relative error is smaller than or equal to μ, it can be concluded that the relative error has converged, and it will output the optimized location and type of dipoles. Otherwise, the number of dipoles will be increased by one and this optimization will be executed again. μ means the minimum decrease of relative error which can be tolerated with an increment in dipole number. The definition of relative error is shown as

$$RE_n = \sqrt{\frac{\sum_{Surface\ n} [(\left|E_z^{scan}\right| - \left|E_z^{fit}\right|)^2 + (\left|E_\varphi^{scan}\right| - \left|E_\varphi^{fit}\right|)^2]}{\sum_{Surface\ n} (\left|E_z^{scan}\right|^2 + \left|E_\varphi^{scan}\right|^2)}} \tag{1}$$

$$RE = \frac{1}{N}\sum_{n=1}^{N} RE_n, \tag{2}$$

where RE_n is the relative error between the measured electric fields and calculated electric fields from equivalent dipoles on surface n, and RE is the overall relative error which is an average of relative error on all surfaces. N is the number of scanning surfaces. N is usually equal to 2, but it can also be 1 when single-surface scanning is adopted.

2.1. IMPROVED BACK-AND-FORTH ITERATION ALGORITHM

The improved back-and-forth iteration algorithm is shown in Figure 3. The algorithm starts with given position and type of dipoles. Assuming that the fields at all scanning points on one surface have the same phase, the initial magnitude and phase of dipoles can be obtained by linear least squares. The dipole set is named as dipole set M.

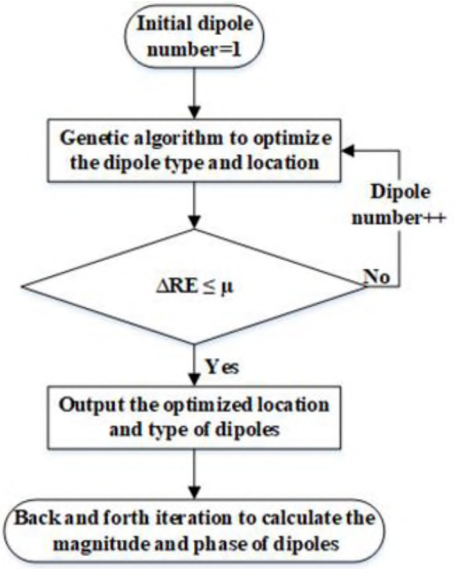

Figure 2. General flow of the method.

Step 1: calculate the electric fields on surface #1 from dipole set M by

$$[E]_{M\times 1} = [T]_{M\times N}[D]_{N\times 1}, \tag{3}$$

where E represents the complex value of electric fields, D represents the complex value of dipoles, and T represents the transfer function relating electric fields on surface #1 to dipoles. T is determined by the location and type of dipoles and the location of scanning points. M is the number of scanning points and N is the number of dipoles.

For cylindrical scanning, (4) can be rewritten as

$$\begin{bmatrix} Ez \\ Ephi \end{bmatrix}_{M\times 1} = \begin{bmatrix} T_{Ez} \\ T_{Ephi} \end{bmatrix}_{M\times N} [D]_{N\times 1}, \tag{4}$$

where T_{Ephi} is calculated by

$$T_{Ephi} = -T_{Ex}\sin(\varphi) + T_{Ey}\cos(\varphi) \tag{5}$$

based on the coordinate transformation from cardinal coordinates to cylindrical coordinates. φ represents the angular coordinate.

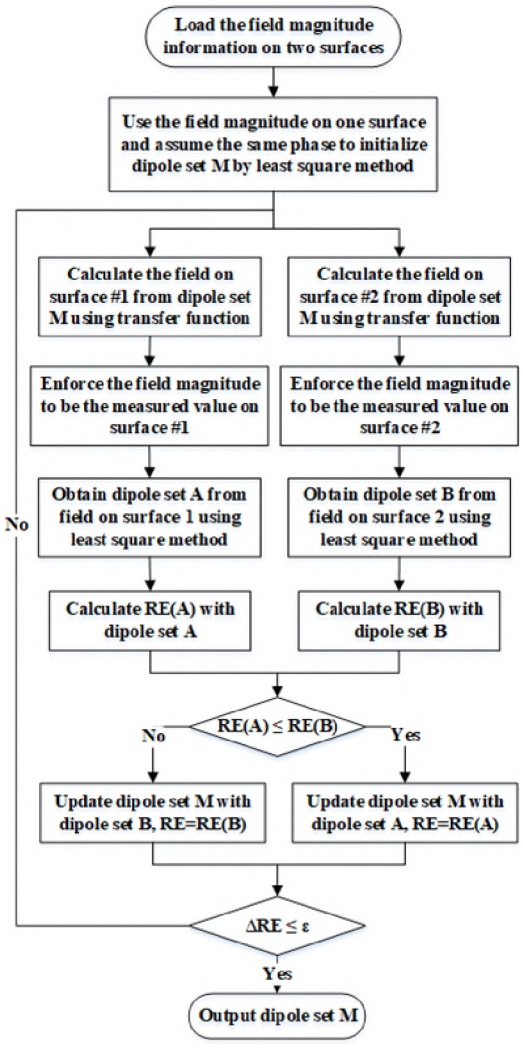

Figure 3. General flow of the improved back-and-forth iteration algorithm for two-surfaces scanning.

Assuming that there is an infinitely large perfect electric conductor (PEC) ground at $z=0$, T_{Ex}, T_{Ey}, and T_{Ez} associated with different dipole types, i.e., *Mx*, *My*, *Mz*, *Px*, *Py*, and *Pz*, can be calculated using equations derived in [13].

Step 2: enforce the magnitude of the electric fields on surface #1 to be the measured magnitude but keep the phase unchanged.

Step 3: use the updated electric fields on surface #1 in step 2 to inversely calculate

the dipole value by linear least squares method as

$$D=(T^T T)^{-1}T^T E. \tag{6}$$

The obtained dipole value is named as dipole set A.

Step 4: calculate the electric fields on surface #1 and #2 from dipole set A using (3). Calculate the *RE* with dipole set A using (1) and (2).

Step 5: calculate the electric fields on surface #2 from dipole set M using (3).

Step 6: enforce magnitude of the electric fields on surface #2 to be the measured magnitude but keep the phase unchanged.

Step 7: use the updated electric fields on surface #2 in step 6 to inversely calculate the dipole magnitude and phase using (6). The obtained dipole value is named as dipole set B.

Step 8: calculate the electric fields on surface #1 and #2 from dipole set B using (3). Calculate the *RE* with dipole set B using (1) and (2).

Step 5~8 can be executed in parallel to *Step 1~4*.

Step 9: compare the *RE* with dipole set A and *RE* with dipole set B. Update the dipole set M with dipole set A or B, whichever gives a smaller *RE*.

The *RE* will be compared with *RE* in the previous iteration. If the decrease of *RE* is smaller than or equal to ε, it can be concluded that *RE* has converged and it will output the obtained magnitude and phase of dipoles. Otherwise, this iteration will be executed again. ε means the minimum decrease of *RE* which can be tolerated with an increment in iteration number.

The main difference between the improved back-and-forth iteration algorithm introduced in this paper and the conventional algorithm is that transformation between

fields on two different surfaces is not needed. The main advantage is that the method can be applied to electromagnetic-field measurement on arbitrarily shaped surfaces. In [17], field transformation from the lower plane to the higher plane is achieved using the plane-wave expansion method. For cylindrical scanning, field transformation from the inner cylindrical surface to the outer cylindrical surface is more complicated. The improved back-and-forth iteration algorithm can be applied in planar, cylindrical, or spherical scanning.

Although field magnitude on two surfaces is usually used to get the dipole value, the algorithm can be adapted as shown in Figure 4 for single-surface scanning. Single-surface scanning can greatly reduce the measurement time.

2.2. GENETIC ALGORITHM

The genetic algorithm is a method based on natural selection, the process that drives biological evolution, for solving both constrained and unconstrained optimization problems. The genetic algorithm repeatedly modifies a population of individual solutions. At each step, the genetic algorithm selects individuals from the current population to be parents and uses them to produce the children for the next generation. Over successive generations, the population "evolves" toward an optimal solution [20]. It is useful in terms of optimization for highly nonlinear problems. The genetic algorithm is used to optimize the dipole type and location in this method.

The objective function to minimize is the relative error defined in (1) and (2). The optimization range for dipole location can be set as the occupied space of the original DUT or radiating structure. The optimization range for dipole type can be set as [Px, Py, Pz, Mx,

My, *Mz*]. It means that the dipole type can be any one of the six kinds. The optimization of dipole type is realized by integer programming. A meaningful optimization range can help us extract dipoles close to the original radiating source and reduce optimization time.

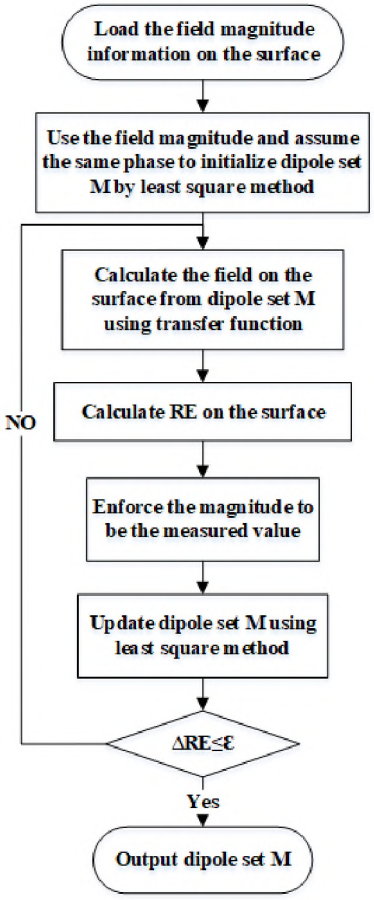

Figure 4. General flow of the improved back-and-forth iteration algorithm for single-surface scanning.

The general flow of the optimization using the genetic algorithm is shown in Figure 5. The algorithm starts with a population of randomly decided individuals for dipole type and location. Then the improved back-and-forth iteration algorithm is used to obtain the magnitude and phase of dipoles for each individual. The objective function for each

individual is evaluated next for selection of parents. Subsequent generations evolve from the current generation through selection, crossover, and mutation to search for new dipole type and location. This procedure will go over and over again until the max number of generations is reached, or the average change of objective function is less than the tolerance. Then the algorithm will stop and return the optimized dipole type, dipole location, and minimized relative error.

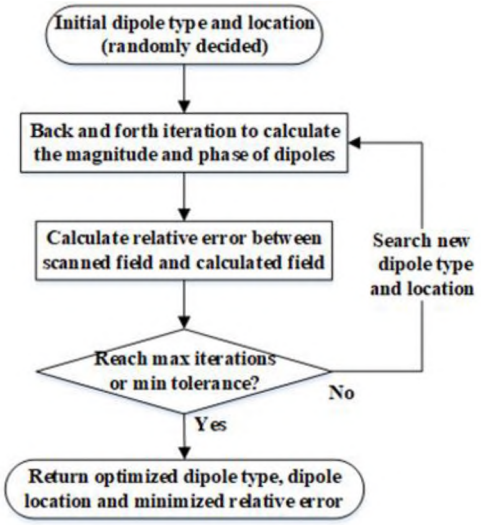

Figure 5. General flow of the genetic algorithm.

3. VALIDATION OF THE METHOD

3.1. SIMULATION DATA WITH INFINITESIMAL DIPOLES AS RADIATING SOURCE

The method is first validated using simulation data with infinitesimal dipoles as the radiating source. The simulation is done in EMCos [21], a MOM-based software. In this case, two infinitesimal dipoles are used as the original radiating source. One *Px* and one

My dipole are placed above the PEC ground with z=0. The *Px* dipole is located at (0.25 m, 0, 1.5 m) with a magnitude of 1 Am and a phase of 90 degrees. The *My* dipole is located at (-0.25 m, 0, 1.5 m) with a magnitude of 100 Vm and a phase of 0 degrees. The magnitude of electric fields (*Ez* and *Ephi*) on two cylindrical surfaces with a radius of 0.5 m and 1 m at 781.25 MHz is used as the input data to the method. The scanning heights are from 1m to 4m with a step of 0.25 m and there are 24 scanning points along the circle with a step of 15 degrees as shown in Figure 6. The two blue arrows represent the two infinitesimal dipoles *Px* and *My*. The aqua dots represent the scanning points along the circle. The optimization range for *x* coordinates of dipole location is from -0.5 to 0.5, the optimization range for *y* coordinates of dipole location is from -0.5 to 0.5, and the optimization range for *z* coordinate of dipole location is from 1 to 2. When the number of dipoles is 2, the extraction results are shown in Table 1. The extracted dipoles are almost the same as the original radiating source in terms of the type, location, and amplitude of the dipoles. The phase difference of the extracted two dipoles is 90 degrees, which is the same as the original dipole source.

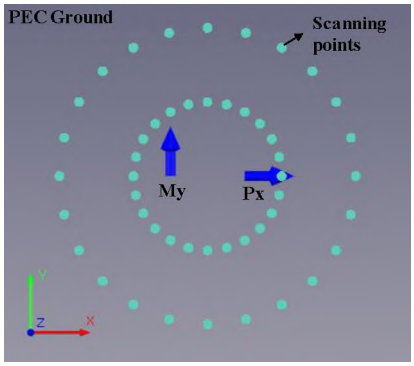

Figure 6. Scanning points along the circle.

Table 1. Comparison between original source and extraction results.

		Original source		Extracted dipoles	
		dipole 1	dipole 2	dipole 1	dipole 2
dipole location (meter)	x	0.25	-0.25	0.25	-0.25
	y	0	0	-1.246e-5	-1.449e-5
	z	1.5	1.5	1.4999	1.4998
dipole type		*Px*	*My*	*Px*	*My*
dipole amplitude		1 Am	100 Vm	0.9999 Am	99.9968 Vm
dipole phase (degree)		90	0	147.0478	57.0494

3.2. SIMULATION DATA WITH WIRE ANTENNA AS RADIATING SOURCE

To prove that this method can extract physics-based dipoles, a half-wavelength wire antenna is used as the original radiating source. The center of the wire antenna is located at (0, 0, 1.5m) and the wire antenna is placed along the z-axis. The excitation voltage is 5 V, 0 degrees. The magnitude of electric fields (*Ez* and *Ephi*) on two cylindrical surfaces with a radius of 0.5m and 1m at 781.25 MHz is used as the input to the method. The scanning points distribution is the same as Section 3.1. The optimization range of dipole location is also the same as Section 3.1. When the number of dipoles is 1, the extracted dipole is a single *Pz* dipole located at (-3.629e-05 m, 2.226e-06 m, 1.4977 m) with a magnitude of 0.0066 and phase of -10.17 degrees. The relative error between the calculated fields from dipole and scanned fields is 0.0339. The extracted dipole is close to the original radiating structure since the current in the original wire antenna flows in the z-direction and the radiating wire antenna is composed of a series of *Pz* dipoles along the wire. Because

the observation surface is far away from wire antenna, a series of *Pz* dipoles along the wire is approximately equivalent to a single *Pz* dipole in the center.

The current along the half-wavelength wire antenna is shown in Figure 7. It can be approximately expressed as

$$I(\mathrm{z}) = I_0 \sin[\frac{2\pi}{\lambda}(\frac{\lambda}{4} - \mathrm{z})],\ -\frac{\lambda}{4} \le z \le \frac{\lambda}{4}, \tag{7}$$

where I_0 is calculated by

$$I_0 = \frac{V}{Z_{in}} = \frac{5\ V}{(73\ +\ j42.5)\ Ohm}. \tag{8}$$

The value of *Pz* dipole is calculated as

$$\int_{-\frac{\lambda}{4}}^{\frac{\lambda}{4}} I(\mathrm{z})dz = \frac{I_0\lambda}{\pi} = \frac{V\lambda}{Z_{in}\pi} = 0.0072\angle -30.2076^{\circ}. \tag{9}$$

The calculated value is close to the value of extracted single Pz dipole.

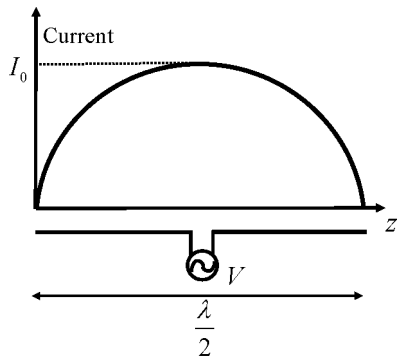

Figure 7. Current along half wavelength wire antenna.

3.3. SIMULATION DATA WITH AN IC EMISSION MODEL AS RADIATING SOURCE

To demonstrate the features of the proposed method, the simulated magnetic fields with only magnitude at 500 MHz above an IC model are used as input to the algorithm. The IC model is shown in Figure 8 and it is exactly the same as the example used in [17]. Two cases are run using this example. One case is that magnetic fields on two planes 9 mm and 12 mm high from the PEC ground are used as input to the algorithm for two-surfaces scanning. The other case is that magnetic fields on one plane 9 mm high from the PEC ground are used as input to the algorithm for single-surface scanning.

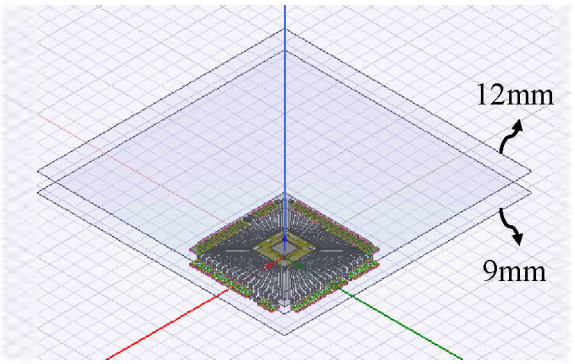

Figure 8. IC emission model.

The relative error and optimization time versus the number of extracted dipoles for the two cases are shown in Figure 9(a). The optimization time is the accumulated time starting from one dipole. Both cases show a close trend for relative error and converge at a relative error around 0.08 when the number of dipoles is 6. The optimization time of the algorithm for two scanning planes is longer than the algorithm for one scanning plane because the iteration algorithm for two scanning planes takes a longer time than the

iteration algorithm for one scanning plane. To extract 6 dipoles, the algorithm for two scanning planes takes 108.6 minutes while the algorithm for one scanning plane takes 74.7 minutes. The reason why two planes are normally used is to ensure that the phase is correctly retrieved and the second plane can be thought of as a validation plane. The relative

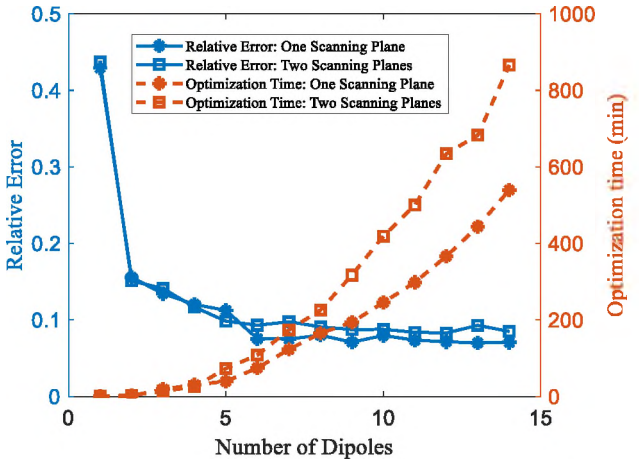

(a)

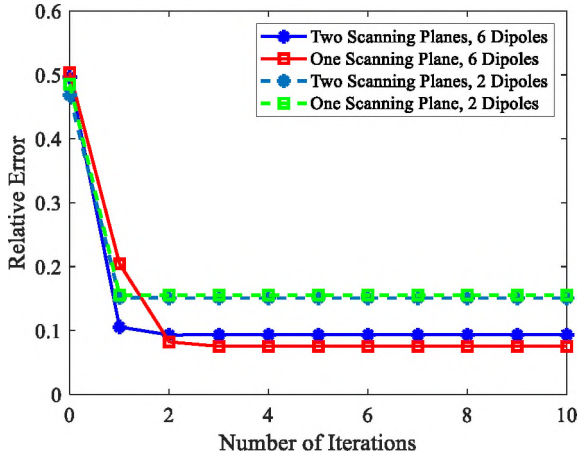

(b)

Figure 9. Comparison between the methods for one scanning plane and two scanning planes. (a)Relative error and optimization time versus dipole number. (b)Relative error during iteration.

error during the iteration process after the location and type of dipoles are optimized is shown in Figure 9(b). The iteration process converges quickly.

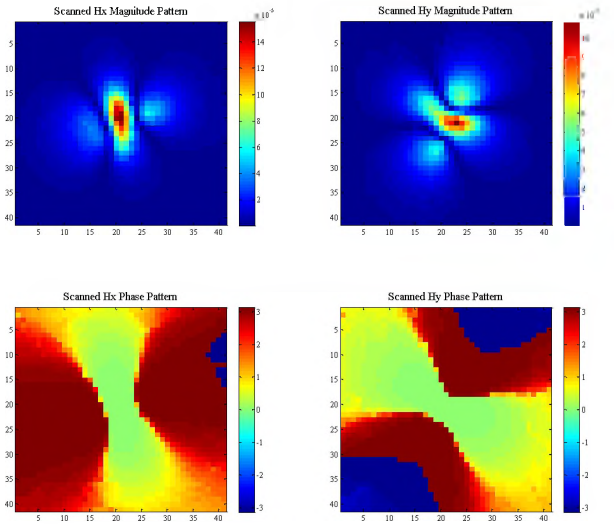

(a)

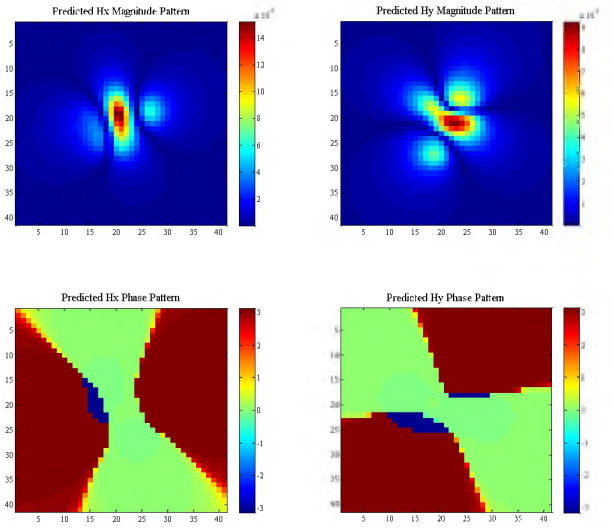

(b)

Figure 10. Comparison between the Magnetic fields on the plane with height of 9 mm (500 MHz, in unit of A/m and degree). (a)Original. (b)Calculated from extracted dipoles.

For the case using two scanning planes, when the number of extracted dipoles is 6, the original and recovered magnetic fields on the plane with a height of 9 mm are shown in Figure 10. The magnitude pattern of recovered magnetic fields matches well with original magnetic fields, and the phase is retrieved correctly.

The comparison between the proposed method and Ji's method [17] is shown in Table 2. In conclusion, the proposed method provides an automatic way to extract dipoles and minimize the number of dipoles. But the optimization takes much more time and the relative error is slightly larger due to the small number of dipoles.

Table 2. Comparison between proposed method and Ji's method.

	Proposed method	Ji's method
Dipole number	6	64*3
Relative error	0.09	0.045
Computation time	108.6 mins	Less than 1 min
Single scanning surface?	Yes	No
Arbitrarily shaped surface?	Yes	No
Automatic?	Yes	No

3.4. MEASUREMENT DATA WITH A CLOCK BUFFER IC AS RADIATING SOURCE

The magnetic fields at 1.6 GHz on a single plane above a clock buffer IC are measured to validate the method for single-plane scanning. The scanning plane is 5 mm

high above the PEC ground. The measurement setup of the near fields is shown in Figure 11. The time-domain waveform is converted to the frequency domain via fast Fourier transform (FFT), and two channels are used to measure phase. Both magnitude and phase are measured using this measurement setup, but only magnitude is used as input to the algorithm. The scanned magnetic-field pattern above the IC is shown in Figure 12(a). The same magnetic fields are also used as input to the method with only genetic algorithm. The comparison between the two methods is shown in Figure 13. The method with only genetic algorithm not only takes a longer time but also converges at a larger relative error. The optimization can fall into local minima due to the large variation range of dipole magnitude. The proposed algorithm converges at 0.07 with 4 dipoles. The calculated magnetic-field pattern from the 4 dipoles is shown in Figure 12(b). The magnitude pattern of recovered magnetic fields matches well with original magnetic fields and the phase is retrieved correctly.

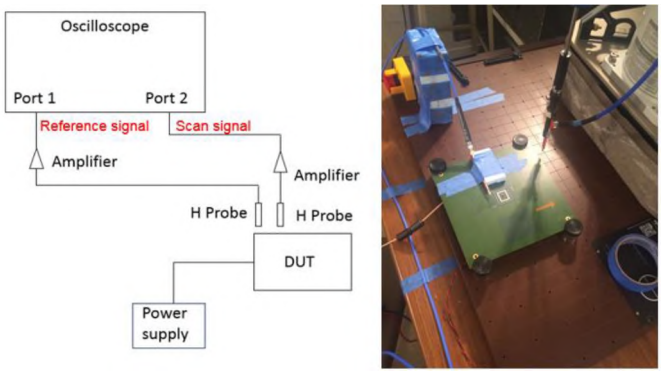

Figure 11. Measurement setup to scan the near fields above clock buffer IC.

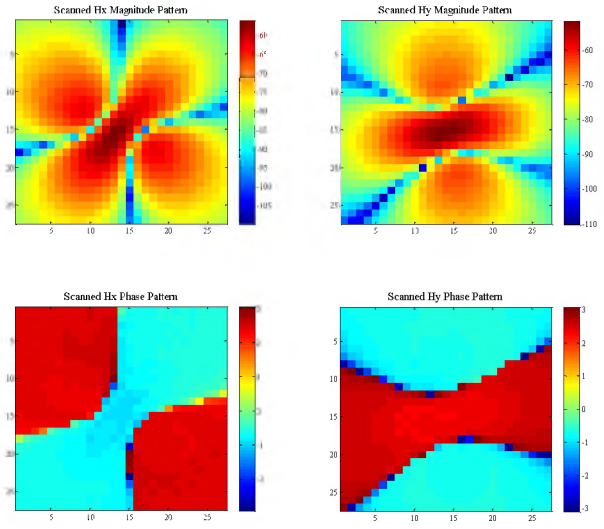

(a)

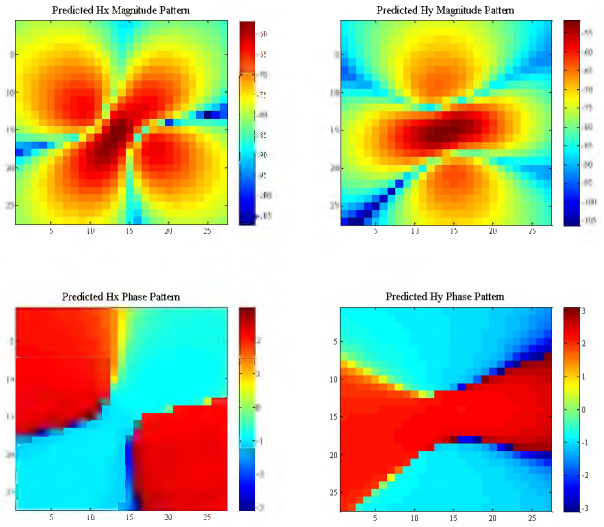

(b)

Figure 12. Magnetic fields above the clock buffer IC (1.6 GHz, in unit of dBA/m and degree). (a)Original. (b)Calculated from extracted dipoles.

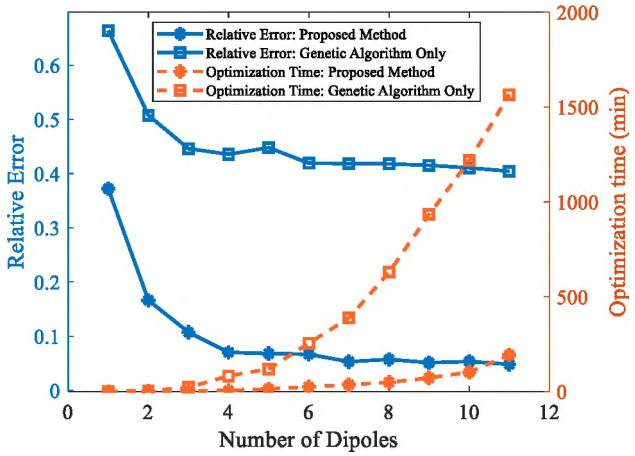

Figure 13. Comparison between the method with only genetic algorithm and the proposed method.

4. CONCLUSION

This paper proposes an improved method to extract dipoles from magnitude-only electromagnetic-field data. Two contributions are made to the current study. The first contribution is that it improves the iteration approach of the back-and-forth iteration algorithm in [17] and enables the algorithm to work for electromagnetic-field data on a single scanning surface and arbitrarily-shaped scanning surfaces. The second contribution is that it combines the genetic algorithm with the back-and-forth iteration algorithm, which makes the algorithm automatic without predetermination of the type and location of dipoles. It also minimizes the number of required dipoles because of the gradual increment of dipole number. But bringing in the genetic algorithm also means increased computation time, especially when the number of extracted dipoles is large. As shown in [5], the radiation from PCB traces can be modeled using a single horizontal magnetic dipole. As explained in [22], the common-mode radiation from PCB with attached cables is typically

caused by an unintentional voltage source driving an EMI antenna similar to wire antenna. Therefore, the algorithm is suitable for EMI applications, where the noise source can be modeled using a few dipoles.

REFERENCES

[1] T. S. Sijher and A. A. Kishk, "Antenna modeling by infinitesimal dipoles using genetic algorithms," *Progress Electromagn. Res.*, vol. PIER 52, pp. 225–254, 2005.

[2] J. R. Regue, M. Ribó, J. M. Garrell, and A. Martín, "A genetic algorithm based method for source identification and far-field radiated emissions prediction from near-field measurements for PCB characterization," *IEEE Trans. Electromagn. Compat.*, vol. 43, no. 4, pp. 520–530, Nov. 2001.

[3] X. Tong, D. Thomas, A. Nothofer, P. Sewell, and C. Christopoulos, "Modeling electromagnetic emissions from printed circuit boards in closed environments using equivalent dipoles," *IEEE Trans. Electromagn. Compat.*, vol. 52, no. 2, pp. 462–470, May 2010.

[4] C. Wu et al., "Estimating the near field coupling from SMPS circuits to a nearby antenna using dipole moments," in *Proc. 2016 IEEE Int. Symp. Electromagn.Compat.*, 2016, pp. 353–357.

[5] Q. Huang, F. Zhang, T. Enomoto, J. Maeshima, K. Araki, and C. Hwang, "Physics-based dipole moment source reconstruction for RFI on a practical cellphone," *IEEE Trans. Electromagn. Compat.*, vol. 59, no. 6, pp. 1693– 1700, Dec. 2017.

[6] S. Lee et al., "Analytical intra-system EMI model using dipole moments and reciprocity," in *Proc. 2018 IEEE Asia-Pac. Electromagn. Compat. Symp.*, May 2018.

[7] Q. Huang et al., "Desense Prediction and Mitigation from DDR Noise Source," in *Proc. IEEE Electromagn. Compat. Symp.*, 2018.

[8] Q. Huang, Y. Liu, L. Li, Y. Wang, C. Wu, and J. Fan, "Radio Frequency Interference Estimation Using Transfer Function Based Dipole Moment Model," in *Proc. IEEE Asia-Pacific Electromagn. Compat. Symp.*, Singapore, 2018, pp.

[9] C. Hwang and Q. Huang, "IC Placement Optimization for RF Interference based on Dipole Moment Sources and Reciprocity" in *Proc. Asia-Pacific Int. Symp. Electromagnetic Compatibility*, Seoul, Korea, 20-23 June 2017, pp. 331-333.

[10] Q. Huang, T. Enomoto, S. Seto, K. Araki, J. Fan, and C. Hwang, "A transfer function based calculation method for radio frequency interference," *IEEE Trans. Electromagn. Compat.*, vol. 61, no. 4, pp. 1280-1288, Aug. 2019.

[11] Y. Wang, S. Wu, Z. Yang, S. Jin, Y. S. Cao, J. Zhang, and J. Fan, " Correcting antenna pattern in offset measurements based on equivalent dipole moments," in *Proc. IEEE Symp. Electromagn. Compat. Signal Integrity*, Aug. 2018.

[12] Y. Vives, C. Arcambal, A. Louis, F. de Daran, P. Eudeline, and B. Mazari, "Modeling magnetic radiations of electronic circuits using near-field scanning method," *IEEE Trans. Electromagn. Compat.*, vol. 49, no. 2, pp. 391–400, May 2007.

[13] Z. Yu, J. A. Mix, S. Sajuyigbe, K. P. Slattery, and J. Fan, "An improved dipole-moment model based on near-field scanning for characterizing near-field coupling and far-field radiation from an IC," *IEEE Trans. Electromagn. Compat.*, vol. 55, no. 1, pp. 97–108, 2013.

[14] F. Benyoubi, L. Pichon, M. Bensetti, Y. Le Bihan and M. Feliachi, "An Efficient Method for Modeling the Magnetic Field Emissions of Power Electronic Equipment From Magnetic Near Field Measurements," in *IEEE Transactions on Electromagnetic Compatibility*, vol. 59, no. 2, pp. 609-617, April 2017.

[15] C. Wu, Z. Sun, Q. Huang, Y. Wang, J. Zhou and J. Fan, "A Method to Extract Physical Dipoles for Radiating Source Characterization and Near Field Coupling Estimation" in *Proc. of IEEE Int. Symp. Electromagn.Compat.*, Aug. 2019.

[16] Y.-F. Shu, X.-C. Wei, J. Fan, R. Yang, and Y.-B. Yang, "An equivalent dipole model hybrid with artificial neural network for electromagnetic interference prediction," *IEEE Trans. Microw. Theory, Techn.*, vol. 67, no. 5, pp. 1790–1797, May 2019.

[17] J. Zhang, and J. Fan, "Source reconstruction for IC radiated emissions based on magnitude-only near-field scanning," *IEEE Trans. Electromagn. Compat.*, vol. 59, no. 2, pp. 557-566, Apr. 2017.

[18] R. W. Gerchberg and W. O. Saxton, "A practical algorithm for the determination of the phase from image and diffraction plane pictures," *Optik*, vol. 35, pp. 237–246, 1972.

[19] Q. Huang and J. Fan, "Machine learning based source reconstruction for RF desense," *IEEE Trans. Electromagn. Compat.*, vol. 60, no. 6, pp. 1640–1647, Dec. 2018.

[20] [Find global minima for highly nonlinear problems. [Online]. Available: https://www.mathworks.com/discovery/genetic-algorithm.html

[21] EMCos Studio. 2018. [Online]. Available: https://www.emcos.com/

[22] D. M. Hockanson, J. L. Drewniak, T. H. Hubing, T. P. Van Doren, F. Sha, and M. Wilhelm, "Investigation of fundamental EMI source mechanisms driving common-mode radiation from printed circuit boards with attached cables," *IEEE Trans. Electromagn. Compat.*, vol. 38, no. 4, pp. 557–566, Nov. 1996.

II. ANALYSIS AND MODELING OF CONDUCTED EMI FROM AN AC-DC POWER SUPPLY IN LED TV UP TO 1 MHZ

Chunyu Wu, Hongseok Kim, Jiayi He, Nicholas Erickson, Sangho Cho, Dohyung Kim, Yeong Hur, David Pommerenke, and Jun Fan

ABSTRACT

Critical conduction mode (CRM) boost power factor correction (PFC) converter is widely used in ac-dc power supplies to achieve high power factor (PF). The switching frequency varies in a half-line cycle. In this paper, both the differential mode (DM) and common mode (CM) electromagnetic interference (EMI) below 1 MHz from the ac-dc power supply in a LED TV is analyzed and modeled. The power supply consists of two parts: CRM boost PFC converter and *LLC* resonant converter. The conducted EMI and noise source voltages are measured in the time domain and then converted to the frequency domain via short-time fast Fourier transform. Through joint time-frequency analysis, the drain-to-source voltage of the power MOSFET in the PFC converter is identified as the dominant noise source of both CM and DM EMI below 1 MHz from the power supply. The EMI current path changes during different periods of the cycle. During most time of a cycle, two diodes of the bridge rectifier are forward biased, and the bridge rectifier can be treated as short circuit. The current paths of DM and CM EMI are explained and modeled by a linear equivalent circuit model. Three parasitic capacitances need to be considered to model the CM EMI in this DUT. From the circuit model, transfer functions relating DM and CM EMI spectrum to noise source voltage spectrum are obtained. The conducted EMI

is predicted by multiplying the measured noise source voltage by the transfer functions. The prediction matches with measurement. The effects of parasitic capacitances on CM EMI are analyzed by simulation and then validated by measurement. The analysis can help with EMI design to reduce the CM EMI.

1. INTRODUCTION

Power factor correction (PFC) circuits are needed in off-line power supplies to shape the input current to be in phase with the input voltage, thus minimizing the line-frequency harmonics of the input current [1]-[3]. This has two main purposes. One purpose is to minimize the current drawn from the mains for the required real power to perform the needed work, thus minimizing power losses and costs associated with the generation and distribution of the power. The other purpose is to minimize interference with other devices being powered from the same source. Stringent regulatory requirements, such as IEC-61000-3-2, have been released to specify the maximum amplitude of line-frequency harmonics of the input current for electrical appliances with an input power of 75W or greater. Active PFC circuits combined with boost converters are the most popular circuits to achieve the PFC function because of low cost, high efficiency, and high power factor. Constant-frequency continuous current mode (CCM) and critical conduction mode (CRM) are two popular control modes used for a boost PFC converter. Boost PFC converters operating in CCM mode are widely adopted in hundreds-watt level applications, while CRM boost PFC converter is suitable for low- and medium-power applications, such as power adaptors, televisions (TV), and so on. A CRM boost PFC converter has the

advantages of zero-current turn-on, no reverse recovery in the diode, relatively simple control circuit, and theoretically achieving unity PF.

Conducted electromagnetic interference (EMI) is strictly regulated internationally by various standards, such as EN55032 in Europe, FCC part 15 in the United States. It is necessary to place an EMI filter [4]-[9] before the CRM boost PFC converter to comply with the standards. Taking EN55032 as an example, IT and multimedia equipment intended primarily for use in a residential environment must meet class B limits which cover the frequency range from 150 kHz to 30 MHz with average and quasi-peak detectors.

The EMI issues from a boost PFC converter have been studied a lot in literature. In [10], the conducted EMI from a 1 kW CCM PFC converter is modeled and predicted. The operating mode of the PFC converter in [10] is different from this paper. Reference [11] studies and predicts the EMI noise from electronic ballasts which consists of a CRM boost PFC converter and a load-resonant half-bridge inverter for fluorescent lamps. However, reference [11] purely models every part of the system and lacks the analysis of dominant noise source, noise current path, etc., which is just the highlight of this paper. The major common-mode (CM) noise sources in a PFC converter for low-power applications are identified and the parasitic capacitances are characterized in [12]. The noise source and EMI model for the ac to dc converter in [12] are different from this paper. Reference [13] predicts the differential-mode (DM) EMI from CRM PFC converters using a mathematical model based on the principle of quasi-peak detection. The mathematical model in [13] is extended in [14] to analytically study the worst-case DM EMI under different input voltage and load conditions and design a DM filter. A more comprehensive study of both CM and DM EMI for the design of EMI filter is carried out in [15]. But the mathematical model in

reference paper [13]-[15] is based on an ideal CRM PFC converter, rather than an actual power supply which contains multiple noise source. Using switching frequency modulation in the reduction of the DM conducted EMI of the boost PFC converter is investigated in [16]. A method using negative capacitance to cancel the CM parasitic capacitance of boost PFC converters is proposed in [17].

In this paper, the conducted EMI from the ac to dc power supply in a LED TV is analyzed. The overall system diagram of the power supply is shown in Figure 1. The power supply uses a two-wire power cord. The power supply consists of two parts: CRM boost PFC converter and *LLC* resonant converter. The *LLC* resonant converter has two main functions. One function is to provide isolation, the other function is to regulate the output voltage of PFC to lower voltage. It also features high efficiency because of the soft-switching operation. The output of the *LLC* resonant converter is referenced to a large metal chassis with a size of 48 inches by 28 inches in the TV. EMI filter is not included in the power supply board during this study to focus on the investigation of the noise source and current path. The operating frequency range of PFC converter is from 190kHz to 250kHz, and the operating frequency of *LLC* resonant converter is 78kHz.

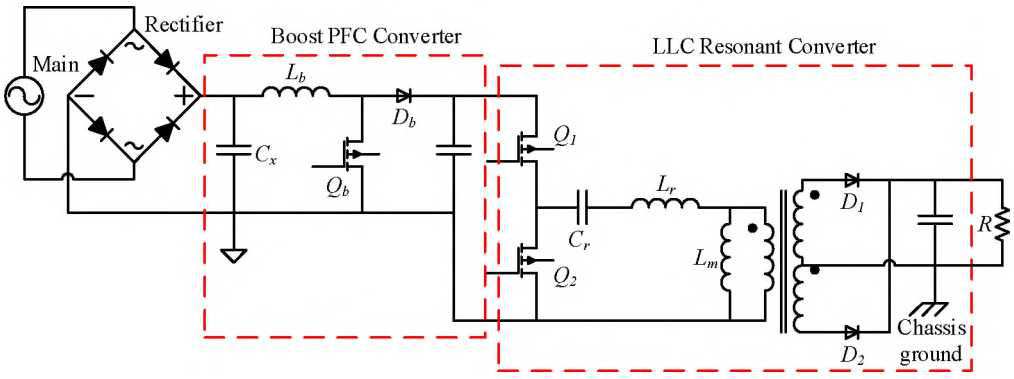

Figure 1. System diagram of the power supply for the LED TV.

Determining the required filter attenuation and corner frequency is an important step for EMI filter design, and the required filter attenuation is mainly decided by the conducted EMI at low frequencies (usually below 1 MHz) [18]. Preliminary measurement also shows that the DM and CM EMI below 1 MHz from the device under test (DUT) exceeds the limits the most. Therefore, the conducted EMI from 150 kHz to 1 MHz is the main focus of this paper.

The novelty of this paper is shown in three ways. Firstly, the conducted EMI from the ac to dc power supply in a commercial product (LED TV) and voltages of multiple noise source are measured by oscilloscope and analyzed using short-time fast Fourier transform (STFFT) to show that DM and CM EMI from PFC converter is dominant below 1 MHz. It is pointed out that the EMI model is different during different periods of the cycle. During most time of the cycle, two diodes of the bridge rectifier are forward biased, and the bridge rectifier can be treated as short circuit. When the ac voltage is crossing zero, at most one diode of the bridge rectifier is forward biased. The separation of DM and CM EMI is done in the time domain without the need of noise separator [19]. Secondly, the EMI model of boost PFC converter in this specific power supply is analyzed. Because of the large floating metal chassis used, the EMI model is different from the previous paper where the metal chassis is usually connected to earth ground and only one capacitance needs to be considered [11], [13]-[15]. Three parasitic capacitances affect the CM EMI in this DUT. Ways to simulate these parasitic capacitances are introduced. Last but not least, the effects of these parasitic capacitances on the CM EMI are analyzed. The analysis can help with EMI design to reduce the CM EMI.

This paper is organized as follows. Section 2 provides the measurement results of the noise source voltage, namely the drain-to-source voltage of power MOSFET in the PFC converter and *LLC* resonant converter. Section 3 describes the measurement setup and provides the measurement results of the conducted EMI from the power supply below 1 MHz. Section 4 explains the noise current path for DM and CM EMI and introduces the EMI model to obtain the transfer function relating DM and CM EMI to the noise source voltage. Section 5 compares the predicted DM and CM EMI spectrum with measurement data. Section 6 analyzes ways to reduce the DM and CM EMI. The last section concludes the paper.

2. MEASUREMENT OF THE NOISE SOURCE VOLTAGE

The drain-to-source voltages of the power MOSFETs in boost PFC converter and *LLC* resonant converter, namely Q_b and Q_2 in Figure 1, are regarded as the noise sources of conducted EMI from the power supply below 1 MHz. The two voltages are directly measured using an oscilloscope with a high voltage differential active probe. The sampling rate should be large enough to avoid aliasing base on Nyquist–Shannon sampling theorem. The time-domain waveforms are processed using STFFT to do time-frequency analysis [20][21]. In STFFT, a long time-domain data set is cut into many small segments, and FFT is applied to each segment to generate its short-term frequency content. The amplitude of FFT v.s. frequency is plotted along the y-axis and aligned in time with its segment along the x-axis, to form an overall spectrogram where the color scale represents the amplitude. The spectrogram shows how the spectrum of signal changes over time. The corresponding

max hold spectrum is the maximum FFT amplitude over all time segments. The resolution bandwidth (RBW) is set as 10 kHz. Kaiser window with a spectral leakage of 0.8 is used. Overlap between adjoining segments is set as 0. As shown in Figure 2(a), the noise source voltage in CRM boost PFC converter features time-varying spectrum because of the time-varying switching frequency. To briefly explain the operation of CRM boost PFC converter, the time-domain waveforms of input ac voltage, rectifier output voltage and boost inductor current are shown in Figure 3. The peak current of boost inductor follows the waveform of rectifier output voltage so that the average input current is generally in phase with the input ac voltage to have high PF. Because of the capacitor Cx after the bridge rectifier, when the input ac voltage crosses zero, the rectifier output voltage will not follow ac voltage. During this period, at most one diode of the rectifier is forward biased. The noise source voltage in *LLC* resonant converter features relatively stable spectrum over time because of the fixed switching frequency as shown in Figure 2(c). The odd harmonics are much larger than the even harmonics because the duty cycle is around 50%. Figure 2(b) and 2(d) are the max hold spectrum of Figure 2(a) and 2(c).

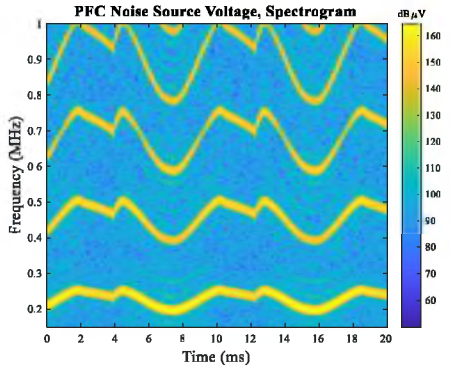

Figure 2. PFC boost converter noise source voltage: (a) spectrogram, (b) max hold spectrum. LLC resonant converter noise source voltage: (c) spectrogram, (d) max hold spectrum.

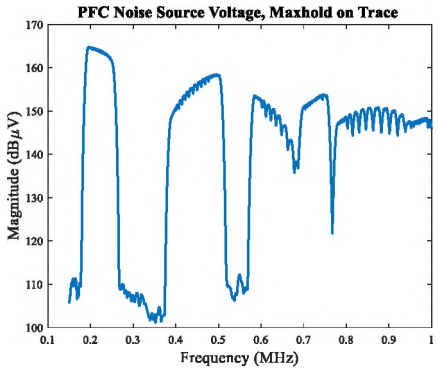

(b)

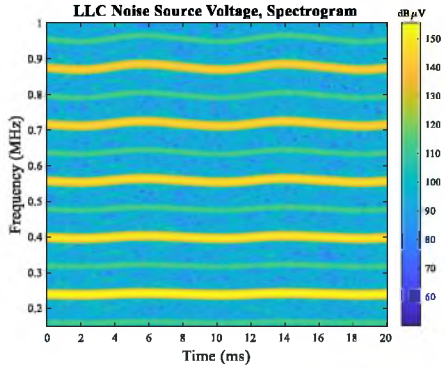

(c)

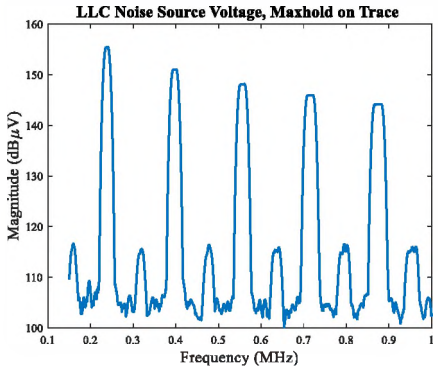

(d)

Figure 2. PFC boost converter noise source voltage: (a) spectrogram, (b) max hold spectrum and LLC resonant converter noise source voltage: (c) spectrogram, (d) max hold spectrum, (Cont.).

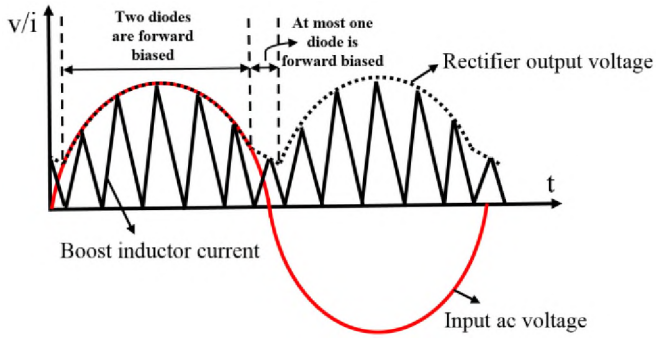

Figure 3. Time-domain waveforms of input ac voltage, rectifier output voltage and boost inductor current.

3. MEASUREMENT OF THE CONDUCTED EMI

Conducted EMI measurement based on EN55032, Class B or FCC Part 15, Subpart B, Class B should be carried out with EMI receiver using both quasi-peak and average detectors. The modeling of EMI receiver with different detector settings can be found extensively in [22]-[24]. This paper focuses on the noise source and current path of the conducted EMI, so modeling of EMI receiver is not within the scope of this paper and the measurements were conducted with oscilloscope instead of EMI receiver to enable time-frequency analysis.

3.1. MEASUREMENT SETUP

The measurement setup is shown in Figure 4. The distance between the TV and vertical earth ground is 40 cm. The height of the wooden table is 80 cm. The power supply board is mounted on the metal chassis which is floating. The power supply board is a two-layer printed circuit board (PCB) where the top layer is for components and the bottom layer is for routing. The distance between the metal chassis and the bottom layer of the

PCB is about 6 mm. Outputs from the two ports of line impedance stabilization network (LISN) are fed into two channels of the oscilloscope. The input impedance of the two channels is set to 50 Ohm. The same attenuators are inserted before the two channels to protect the oscilloscope. The time-domain waveforms of the two channels are recorded during the same time intervals with adequate time length. The oscilloscope setting and STFFT setting should be the same as Section 2.

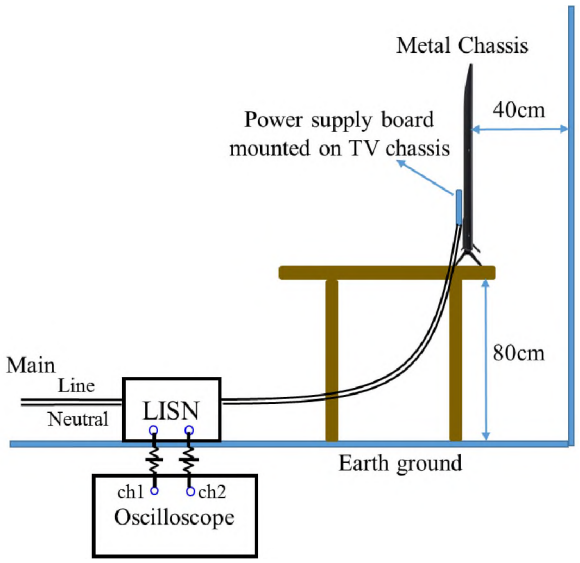

Figure 4. Measurement setup of the conducted EMI.

3.2. MEASUREMENT RESULTS

The DM and CM voltages are calculated as

$$V_{dm} = \frac{V_1 - V_2}{2}, \tag{1}$$

$$V_{cm} = \frac{V_1 + V_2}{2}, \tag{2}$$

where V_1 and V_2 are the measured time-domain waveforms from the two different ports of the LISN. V_1 and V_2 should not include the effects of attenuators before oscilloscope.

The STFFT results of V_1, V_2, V_{dm}, and V_{cm} are shown in Figure 5. In the spectrograms, the component with time-varying frequency is the conducted EMI from the PFC converter and the component with fixed frequency is the conducted EMI from the *LLC* resonant converter based on the measurement results of noise source voltage in Figure 2. Based on the measurement results in Figure 5(a) and 5(b), the spectrograms of V_1 and V_2 are almost the same. In Figure 5(c), only the component with time-varying frequency is seen. In Figure 5(d), both the component with time-varying frequency and the component with fixed frequency are seen and they have the same color. It can be concluded that the DM EMI from boost PFC converter is dominant while the CM EMI from boost PFC converter and *LLC* resonant converter has the same level of magnitude. When it goes to max hold, CM EMI from boost PFC converter shows a larger frequency range and

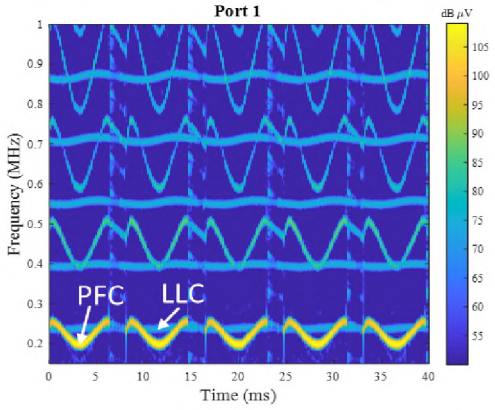

(a)

Figure 5. Measured conducted EMI spectrograms: (a) port 1, (b) port 2, (c) DM voltage, and (d) CM voltage.

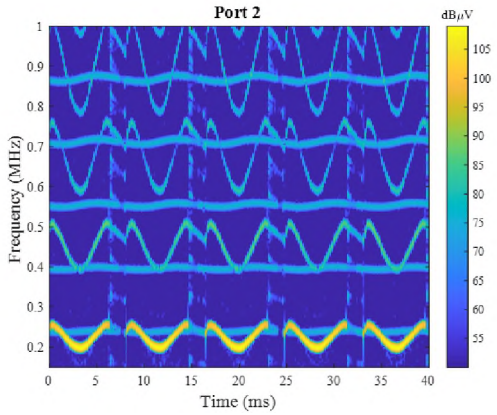

(b)

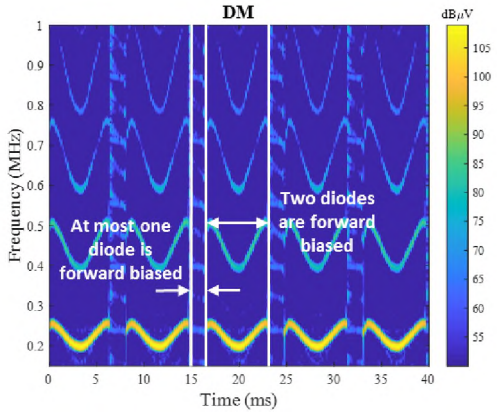

(c)

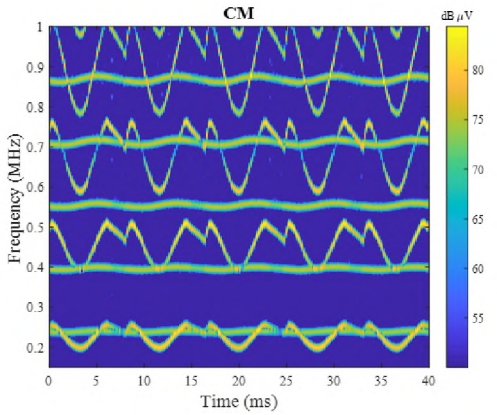

(d)

Figure 5. Measured conducted EMI spectrograms: (a) port 1, (b) port 2, (c) DM voltage, and (d) CM voltage, (Cont.).

dominates. Thus, this paper mainly studies the DM and CM EMI from the boost PFC converter.

If the maximum value over time at each frequency is recorded, the max hold spectrum of a single port (V_1 or V_2), DM, and CM EMI spectrograms can be obtained as shown in Figure 6. The single port (V_1 or V_2) max hold result is also compared with the measurement result when the LISN output voltage V_1 is directly fed into a spectrum analyzer and the other port is terminated with 50 ohm. The spectrum analyzer is set with RBW of 10 kHz, positive peak detector, and max hold on trace. As shown in Figure 6, they match well, which validates that the time domain processing is correct. From the max hold results, it can also be concluded that below 500 kHz, the DM EMI levels are larger than the CM EMI levels. Above 500 kHz, the CM EMI levels are larger than the DM EMI levels.

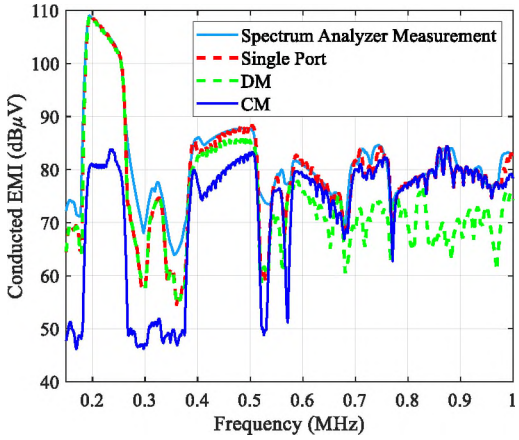

Figure 6. Max hold spectrum of conducted EMI.

4. EMI MODEL

The DM and CM EMI have different current paths. DM EMI comes from the normal operation of the power electronics circuit, while the CM EMI is caused by the parasitic capacitances. Three parasitic capacitances C_{p1}, C_{p2}, and C_{p3} play an important role in determining the CM EMI. C_{p1} represents the parasitic capacitance between the drain side of the power MOSFET and the metal chassis. The drain side of power MOSFET usually has a large layout area for heat dissipation, but this also results in a relatively large parasitic capacitance. C_{p2} represents the parasitic capacitance between the metal chassis and earth ground. Although the distance between metal chassis and vertical earth ground is large, the large area of metal chassis leads to a large parasitic capacitance. C_{p3} represents the parasitic capacitance between the power ground and metal chassis. The EMI current path is also different during different periods of the cycle. When two diodes of the bridge rectifier are forward biased and conducting current, the current path of conducted EMI is shown in Figure 7. The blue dotted line shows the current path of DM EMI and the red dotted line shows the current path of CM EMI. The bridge rectifier can be considered as short circuit for conducted EMI. When the ac voltage is crossing zero, and the absolute value of ac voltage is smaller than the voltage across capacitor C_x, at most one diode of the bridge rectifier is forward biased. The current path for conducted EMI is different from Figure 7. Since the current path for DM EMI shown in Figure 7 does not exist anymore, the DM EMI caused by the PFC converter becomes much smaller during this period as seen in Figure 5(c). When it comes to max hold spectrum below 1 MHz, this short time can be neglected.

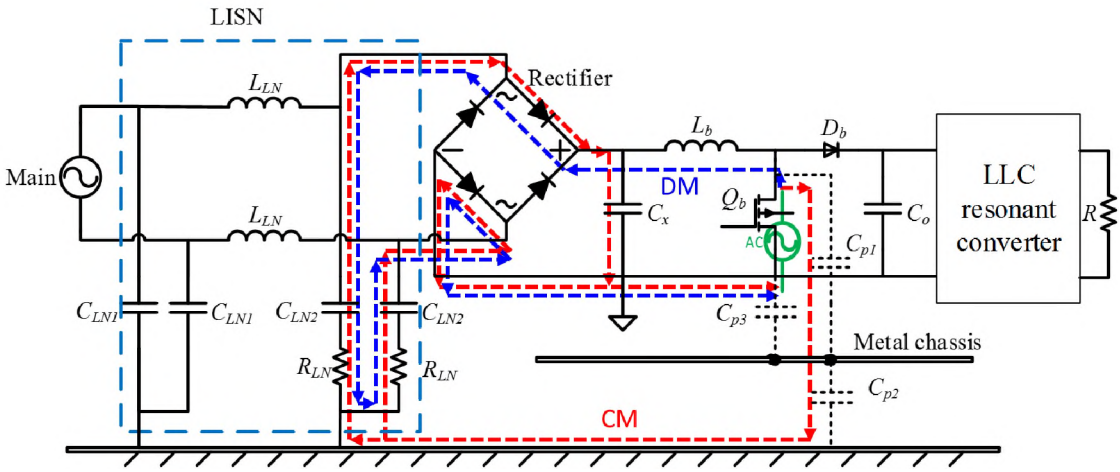

Figure 7. Dominant DM and CM EMI current paths when two diodes of the bridge rectifier are forward biased.

Based on the technique developed in [25], the EMI model which includes the noise source and all linear circuit elements which affect the conducted EMI can be obtained by applying substitution theory as shown in Figure 8. The parasitic inductance and resistance of C_x are taken into account to be more accurate since the measured self-resonant frequency

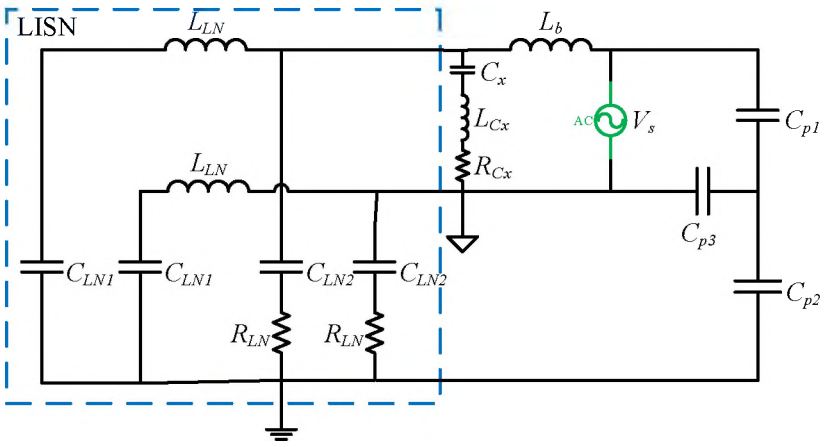

Figure 8. EMI model emphasizing the identified major noise current paths.

of C_x is close to 1 MHz. In the EMI model, L_{LN} = 50 µH, C_{LN1} = 1 µF, C_{LN2} = 0.1 µF, R_{LN} = 50 Ω, L_b = 239 µH, C_x = 0.85 µF, L_{Cx} = 23.7 nH, and R_{Cx} = 0.076 Ω, respectively.

The parasitic capacitances C_{p1}, C_{p2}, and C_{p3} are simulated using ANSYS Q3D Extractor [26] or EMCoS Low Frequency Electric Field Solver [27]. The simulation model to simulate C_{p2} is shown in Figure 9. Based on the simulation results, C_{p1} = 4.0 pF, C_{p2} =58.4 pF, and C_{p3} = 10.0 pF.

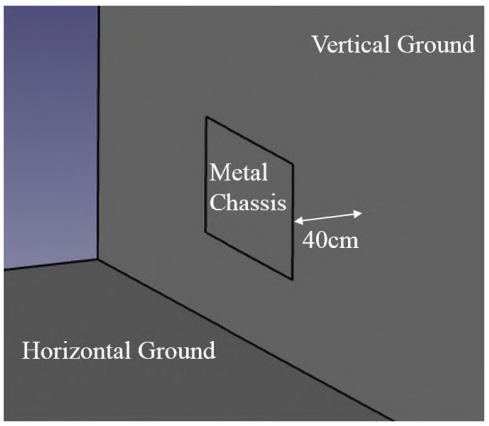

Figure 9. Simulation model to estimate C_{p2} (the capacitance between the metal chassis and ground).

The transfer functions relating DM and CM EMI to noise source voltage Hdm and Hcm are defined as

$$H_{dm} = \frac{V_{dm}}{V_s} = \frac{V_1 - V_2}{2V_s}, \tag{3}$$

$$H_{cm} = \frac{V_{cm}}{V_s} = \frac{V_1 + V_2}{2V_s}, \tag{4}$$

where V_1 and V_2 are the voltages across two LISN resistors and Vs is the noise source voltage.

The transfer functions can be easily calculated using ac small-signal analysis of the SPICE circuit simulator. The simulated transfer functions versus frequency are shown in Figure 10. As the frequency increases, H_{dm} gradually decreases while H_{cm} increases. This is because the impedance of boost converter inductor L_b increases with frequency while the impedance of parasitic capacitances decreases with frequency. Below 500 kHz, H_{dm} is larger than H_{cm}. Above 500 kHz, H_{cm} becomes larger than H_{dm}. This is similar to what is observed in the measurement results in Section 2.

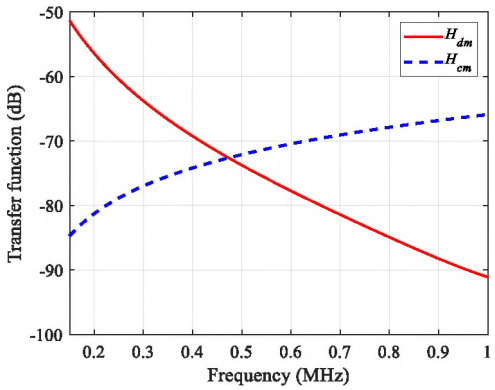

Figure 10. Transfer functions H_{dm} and H_{cm}.

5. PREDICTION OF THE DM AND CM EMI SPECTRUM

After the transfer functions H_{dm} and H_{cm} are obtained by circuit simulation, and the max hold spectrum of the noise source voltage is obtained by measurement and STFFT, the DM and CM EMI spectrum can be predicted by

$$V_{dm}^{pred} = H_{dm}^{sim} \times Vs^{mea}, \tag{5}$$

$$V_{cm}^{pred} = H_{cm}^{sim} \times Vs^{mea}, \tag{6}$$

where H_{dm}^{sim} and H_{cm}^{sim} are the simulated transfer functions relating DM and CM EMI to noise source voltage from EMI model, and Vs^{mea} is the measured max hold spectrum of the noise source voltage, namely the drain-to-source voltage of power MOSFET in boost PFC converter.

The comparison between predicted and measured DM and CM EMI spectrum is shown in Figure 11. They match well in both DM and CM EMI spectrum, which validates the EMI Model. At higher frequencies, the conducted EMI from the *LLC* resonant converter cannot be neglected anymore, so the modeling in this paper will not work at higher frequencies. Modeling of the conducted EMI from the *LLC* resonant converter will be further explored. The predicted CM EMI is a little bit larger than the measured CM EMI. This is because the value of C_{p3} used in the EMI model is smaller than reality. The parasitic capacitance between power ground and chassis is not only from the layout area of power ground, but also from other places, such as the inter-winding capacitance of the

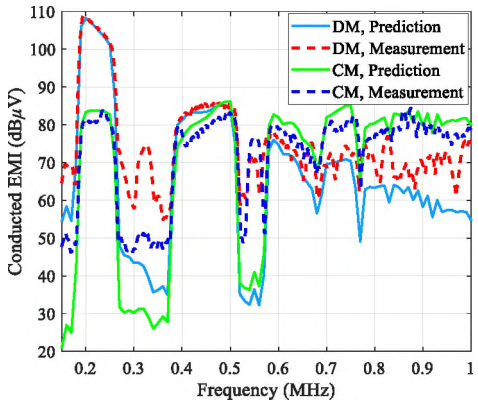

Figure 11. Comparison between prediction and measurement of conducted EMI.

power transformer in the *LLC* resonant converter because the output of *LLC* resonant converter is grounded to the chassis ground.

Although in this paper, the DM and CM EMI spectrum is predicted for the specific TV sample, specific test arrangement, and specific instrument setting, the method can be considered as universal. For example, if the quasi-peak and average detector model is used, the conducted EMI using EMI receiver with standard instrument setting can be predicted. Besides, if the distance between the metal chassis and vertical earth ground is changed to 80 cm, only C_{p3} needs to be changed to predict the conducted EMI in this new test arrangement. The EMI model helps understand the mechanism of the conducted EMI.

6. METHODS TO REDUCE THE DM AND CM EMI

6.1. EMI FILTER

EMI filter is a must for the product to pass the stringent conducted limits. The EMI filter provides a large attenuation of the DM and CM EMI. To evaluate the performance of

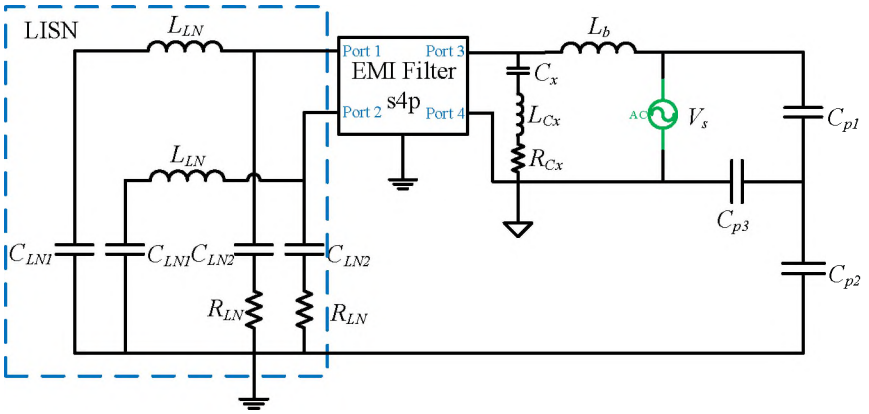

Figure 12. EMI model with EMI filter.

the EMI filter, the scattering parameters of the EMI filter can be measured and the measured s4p file can be imported into the EMI model to simulate the transfer function with EMI filter as shown in Figure 12. The DM and CM EMI spectrum with EMI filter can be then predicted.

6.2. EFFECTS OF THE PARASITIC CAPACITANCE BETWEEN THE DRAIN SIDE OF THE POWER MOSFET AND THE METAL CHASSIS

To analyze the effects of C_{p1} on the CM EMI, the transfer function H_{cm} with different C_{p1} is shown in Figure 13(a). As C_{p1} increases, H_{cm} will increase, thus the CM EMI will increase. To analyze the sensitivity of H_{cm} to $Cp1$, H_{cm} at 500 kHz versus C_{p1} is shown in Figure 13(b). H_{cm} is more sensitive to C_{p1} with a lower value of C_{p1}. Since C_{p1} is about 4 pF in this specific DUT, H_{cm} is very sensitive to C_{p1} under this condition. To reduce C_{p1}, the layout area of the drain side of power MOSFET should be minimized and the distance between layout and metal chassis should be maximized. In practical design, there are other factors to consider other than EMI. For example, a larger layout area of the drain

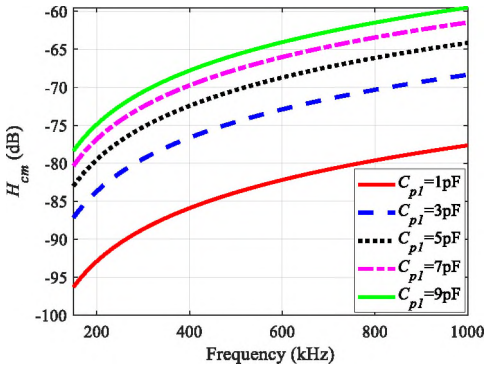

(a)

Figure 13. Effects of C_{p1}. (a) H_{cm} versus frequency with different C_{p1}. (b) H_{cm} @ 500 kHz versus C_{p1}.

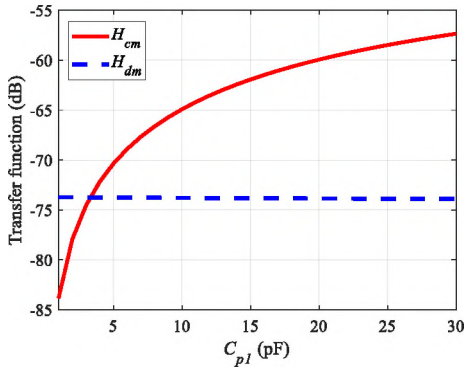

(b)

Figure 13. Effects of C_{p1}. (a) H_{cm} versus frequency with different C_{p1}. (b) H_{cm} @ 500 kHz versus C_{p1}, (Cont.).

side of power MOSFET is needed for smaller conduction loss and heat dissipation. A smaller distance between the layout and metal chassis means a more compact design. Therefore, there is always a compromise between these factors and EMI issues.

6.3. EFFECTS OF THE PARASITIC CAPACITANCE BETWEEN THE METAL CHASSIS AND EARTH GROUND

Similarly, H_{cm} with different C_{p2} is shown in Figure 14(a) to analyze the effect of C_{p2} on the CM EMI. As C_{p2} increases, H_{cm} will increase. H_{cm} at 500 kHz versus C_{p2} is shown in Figure 14(b). H_{cm} is more sensitive to C_{p2} with a lower value of C_{p2}. Because C_{p2} is about 58 pF, H_{cm} is not sensitive to C_{p2} under this condition. The reason is that C_{p1} and C_{p2} are in series if C_{p3} is neglected (C_{p3} is small). And the series impedance is decided by the smaller capacitance, namely C_{p1}. Until the value of C_{p2} becomes closer to the value of C_{p1}, the CM EMI will become more sensitive to C_{p2}. To verify this analysis, the conducted EMI is measured when the distance between metal chassis and the vertical ground is changed to 80 cm. C_{p2} is simulated to be 48.42 pF in this new arrangement. The predicted

EMI is compared with measured EMI in Figure 15. They show good agreement with each other. Both DM and CM EMI do not change when the distance between metal chassis and the vertical ground is changed from 40 cm to 80 cm.

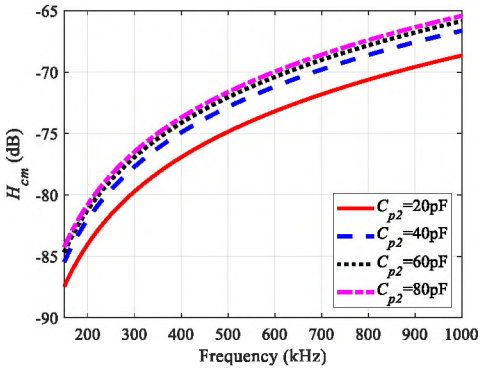

(a)

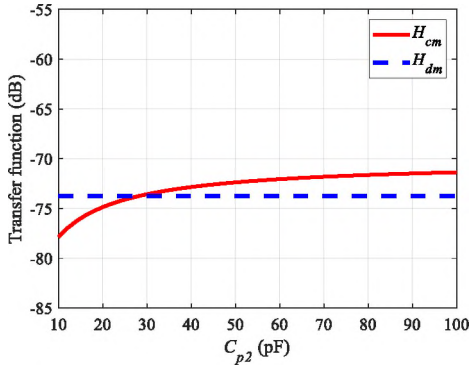

(b)

Figure 14. Effects of C_{p2}. (a) H_{cm} versus frequency with different C_{p2}. (b) H_{cm} @ 500 kHz versus C_{p2}.

6.4. EFFECTS OF THE PARASITIC CAPACITANCE BETWEEN THE POWER GROUND AND METAL CHASSIS

H_{cm} with different C_{p3} is shown in Figure 16(a). H_{cm} at 500 kHz versus C_{p3} is shown in Figure 16(b). As C_{p3} increases, H_{cm} will decrease. A lumped capacitor can be added

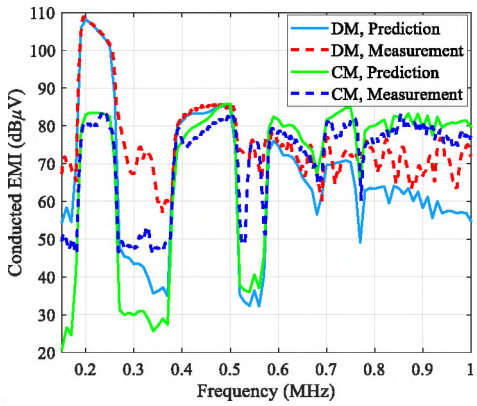

Figure 15. Comparison between prediction and measurement of conducted EMI when the distance between metal chassis and the vertical ground is 80 cm.

between the power ground and chassis ground in the power supply board to increase C_{p3}, thus reducing the CM EMI. However, there will be safety issues caused by large leakage current from the primary side to the secondary side if *Cp3* is excessively large. In this specific DUT, a capacitor measured as 86 pF is added between the power ground and chassis ground to reduce the CM EMI. The conducted EMI with the capacitor added is measured to verify its effects. The measured CM EMI together with the predicted result is shown in Figure 17. The capacitor reduces the CM EMI below 1 MHz by around 6 dB. The measured conducted EMI matches well with prediction.

7. CONCLUSIONS

In this paper, the conducted EMI below 1 MHz from the ac to dc power supply in a LED TV is analyzed and modeled. STFFT is used to analyze the noise source voltage and conducted EMI. The drain-to-source voltage of power MOSFET in the PFC converter

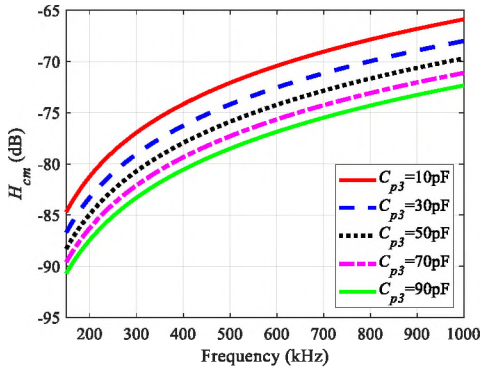

(a)

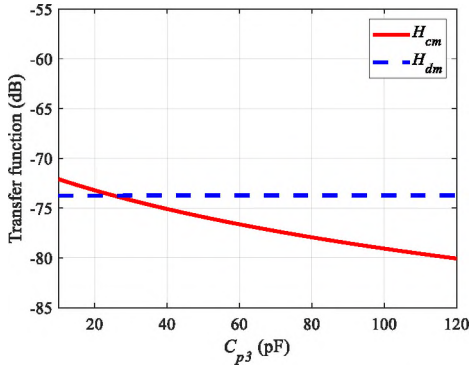

(b)

Figure 16. Effects of C_{p3}. (a) H_{cm} versus frequency with different C_{p3}. (b) H_{cm} @ 500 kHz versus C_{p3}.

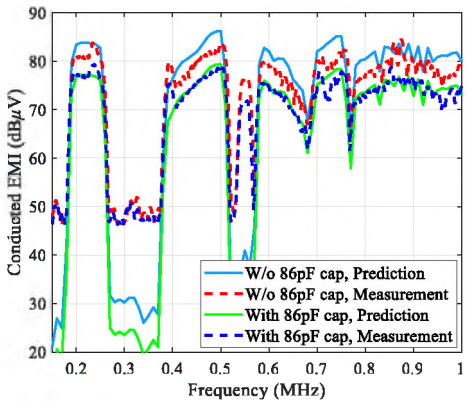

Figure 17. Comparison between prediction and measurement of CM EMI with and without 86pF capacitor.

is identified as the dominant noise source of both DM and CM EMI below 1 MHz. The EMI current path is different during different periods of the cycle. During most time of the cycle, two diodes of the bridge rectifier are forward biased. When the ac voltage is crossing zero, at most one diode of the bridge rectifier is forward biased, the DM EMI will be much smaller. This short time can be neglected when we consider the max hold spectrum. When the bridge rectifier is forward biased, the bridge rectifier can be treated as short circuit, and the current paths of DM and CM EMI are explained and modeled by a linear equivalent circuit model. Three parasitic capacitances need to be considered to model the CM EMI in this DUT. From the circuit model, the transfer function relating DM and CM EMI spectrum to noise source voltage spectrum are obtained. The conducted EMI is predicted by multiplying the measured noise source voltage by the transfer function. The prediction matches well with measurement. The effects of parasitic capacitances C_{p1}, C_{p2}, and C_{p3} on CM EMI are analyzed by simulation and then validated by measurement. The analysis can help with EMI design to reduce the CM EMI.

REFERENCES

[1] J. S. Lai and D Chen, "Design consideration for power factor correction boost converter operating at the boundary of continuous conduction mode and discontinuous conduction mode," in *Proc. IEEE Appl. Power Electr. Conf. Expo.*, Mar. 1993, pp. 267–273.

[2] J. Zhang, J. Shao, P. Xu, F. C. Lee, and M. M. Jovanovic, "Evaluation of input current in the critical mode boost PFC converter for distributed power systems," in *Proc. IEEE Appl. Power Electr. Conf. Expo.*, Anaheim, CA, Mar. 2001, pp. 130–136.

[3] Power Factor Correction (PFC) Handbook. [Online]. Available: https://www.onsemi.com/pub/Collateral/HBD853-D.PDF.

[4] M. Kumar and V. Agarwal, "Power line filter design for conducted electromagnetic interference using time-domain measurements," *IEEE Trans. Electromagn. Compat.*, vol. 48, no. 1, pp. 178–186, Feb. 2006.

[5] V. Tarateeraseth, S. Kye Yak, F. G. Canavero, and R. W. Chang, "Systematic electromagnetic interference filter design based on information from in-circuit impedance measurements," *IEEE Trans. Electromagn. Compat.*, vol. 52, no. 3, pp. 588–598, Aug. 2010.

[6] W. Chen, X. Yang, and Z. Wang, "An active EMI filtering technique for improving passive filter low-frequency performance," *IEEE Trans. Electromagn. Compat.*, vol. 48, no. 1, pp. 172–177, Feb. 2006.

[7] W. Chen, W. Zhang, X. Yang, Z. Sheng, and Z. Wang, "An experimental study of common- and differential-mode active EMI filter compensation characteristics," *IEEE Trans. Electromagn. Compat.*, vol. 51, no. 3, pp. 683–691, Aug. 2009.

[8] D. Shin et al., "Analysis and design guide of active EMI filter in a compact package for reduction of common-mode conducted emissions," *IEEE Trans. Electromagn. Compat.*, vol. 57, no. 4, pp. 660–671, Aug. 2015.

[9] A. Perez, A. M. Sanchez, J. R. Regue, M. Ribo, P. Rodriguez-Cepeda, F. J. Pajares, "Characterization of power-line filters and electronic equipment for prediction of conducted emissions," *IEEE Trans. Electromagn. Compat.*, vol. 50, no. 3, Aug. 2008.

[10] L. Yang, "Modeling and characterization of a 1 KW CCM PFC converter for conducted EMI prediction," in *Proc. Appl. Power Electr. Conf.*, 2004, pp. 763–769.

[11] F. Giezendanner, J. Biela, J. W. Kolar, and S. Zudrell-Koch, "EMI noise prediction for electronic ballasts," *IEEE Trans. Power Electron.*, vol. 25, no. 8, pp. 2133–2141, Aug. 2010.

[12] P. J. Kong, Y. Jiang, and F. C. Lee, "Common mode EMI noise characteristics of low-power AC–DC converters," *IEEE Trans. Power Electron.*, vol. 27, no. 2, pp. 731–738, Feb. 2012.

[13] Z. Wang, S. Wang, C. Wang, F. C. Lee, and P. Kong, "DM EMI noise prediction for constant on-time, critical mode power factor correction converters," *IEEE Trans. Power Electron.*, vol. 27, no. 7, pp. 3150–3157, Jul. 2012.

[14] F. Yang, X. Ruan, Q. Ji, and Z. Ye, "Input differential-mode EMI of CRM boost PFC converter," *IEEE Trans. Power Electron.*, vol. 28, no. 3, pp. 1177–1188, Mar. 2013.

[15] J. Qing, R. Xinbo, and Y. Zhihong, "The worst conducted EMI spectrum of critical conduction mode boost PFC converter," *IEEE Trans. Power Electron.*, vol. 30, no. 3, pp. 1230–1241, Mar. 2015.

[16] R. Morrison, "The effect of switching frequency modulation on the differential-mode conducted interference of the boost power-factor correction converter," *IEEE Trans. Electromagn. Compat.*, vol. 49, no. 3, pp. 526–536, Aug. 2007.

[17] S. Wang and F. C. Lee, "Common-mode noise reduction for power factor correction circuit with parasitic capacitance cancellation," *IEEE Trans. Electromagn. Compat.*, vol. 49, no. 3, pp. 537–542, Aug. 2007.

[18] EMC/EMI Filter Design with RB Common-Mode Chokes. [Online]. Available:https://www.schaffner.com/fileadmin/media/downloads/application_note/Schaffner_AN_RB_common_chockes.pdf.

[19] S. Wang, F. C. Lee, and W. G. Odendaal, "Characterization, evaluation, and design of noise separator for conducted EMI noise diagnosis," *IEEE Trans. Power Electron.*, vol. 20, no. 4, pp. 974–982, Jul. 2005.

[20] Analyze signals in the frequency and time-frequency domains - MATLAB pspectrum. [Online]. Available: https://www.mathworks.com/help/signal/ref/pspectrum.html.

[21] W. Pan and D. J. Pommerenke, "EMI failure Analysis Techniques: II Joint Time-frequency analysis," *IEEE EMC Society Newsletters*, vol. 226, pp. 31-34, 2010.

[22] F. Krug and P. Russer, "Quasi-Peak Detector Model for a Time-Domain Measurement System," *IEEE Trans. Electromagn. Compat.*, vol. 47, no. 2, pp. 320–326, May 2005.

[23] K. Hoermaier, H. Zangl, and H. Zojer, "An EMI Receiver Model to Evaluate Electromagnetic Emissions by Simulation," in *IEEE International Instrumentation and Measurement Technology Conference (I2MTC)*, Graz, May 2012, pp. 2558–2562.

[24] T. Karaca, B. Deutschmann, and G. Winkler, "EMI-receiver simulation model with quasi-peak detector," in *Proc. IEEE Int. Symp. Electromagn. Compat.*, 2015, pp. 891–896.

[25] S. Wang, P. Kong, and F. C. Lee, "Common mode noise reduction for boost converters using general balance technique," *IEEE Trans. Power Electron.*, vol. 22, no. 4, pp. 1410–1416, Jul. 2007.

[26] ANSYS Q3D Extractor. 2019. [Online]. Available: https://www.ansys.com/products/electronics/ansys-q3d-extractor.

[27] EMCos Studio. 2019. [Online]. Available: https://www.emcos.com/.

III. ANALYSIS AND MODELING OF THE CONDUCTED COMMON-MODE EMI FROM WIRELESS POWER TRANSFER SYSTEMS FOR MOBILE APPLICATIONS

Chunyu Wu, Hongseok Kim, Srinath Penugonda, and Jun Fan

ABSTRACT

Wireless power transfer (WPT) is a safe and convenient technology for battery charging thanks to the elimination of electrical contact. Despite the great advantages, the electromagnetic interference (EMI) noise generated by the WPT system will degrade the performance of nearby electrical circuits. In particular, common-mode (CM) EMI noise generated by the WPT system will conduct along the cable and radiate in the high frequency, thus becoming one of the concerns. In this paper, the noise source and current path of the conducted CM EMI noise from a Qi-compliant WPT system for mobile applications are analyzed. The transfer function relating the CM EMI noise to the noise source voltage is derived analytically in the frequency domain. The noise source voltage is measured in the time domain and then converted to the frequency domain via fast Fourier transform (FFT). The conducted CM EMI spectrum is predicted by multiplying the spectrum of noise source voltage by the transfer function. The prediction matches well with measurement. The analysis and modeling explain the mechanism of the CM EMI noise and provide guidelines to reduce the CM EMI noise.

1. INTRODUCTION

Wireless power transfer (WPT) is the transmission of electrical energy without wires as a physical link. It is a safe and convenient technology to charge batteries because it is unaffected in a wet or dusty environment and there is no need to constantly plug and unplug the device from the charging system. Because of its advantages, WPT has been widely deployed in domestic and industrial applications, such as mobile devices, medical implants, and electric vehicles (EV) [1]-[6]. WPT standards, such as Qi from Wireless Power Consortium [7] and Rezence from the Alliance for Wireless Power (A4WP) [8], have been proposed to help commercialize the technology.

Electromagnetic compatibility (EMC) is a significant challenge to the design of WPT systems for EV. Due to the air gap between the coils and large coil current, magnetic field leakage is strong. The strong electromagnetic field (EMF) will not only interfere the automotive electronics such as AM radio, automotive sensors, and analog-to-digital (ADC) converter at the harmonics of switching frequency, but also cause harm to the human body under long-term exposure. Thus, heavy shielding materials are required to shield the strong magnetic field. Coil design and measurement methods are presented in [9] to achieve high efficiency and low EMF. In [10], a new automotive tightly coupled handheld resonant magnetic field (HHRMF) charger operating at 20 kHz with low EMF and high efficiency is designed. A novel three-phase power line in a WPT system for the reduction of the leakage EMF is proposed in [11]. The electromagnetic exposure in an 85 kHz WPT system for EV is evaluated in [12].

Although the coil current in WPT systems for mobile applications is not as large as automotive applications, longer charging distance and larger output power pursued by researchers and industries may also cause EMF leakage and electromagnetic interference (EMI) issues. An investigation of the EM radiated emission and interference from WPT systems using resonant magnetic field coupling with multi-coil configurations is reported in [13]. Yeonje *et al.* propose a novel thin dual-layer printed circuit board (PCB) metamaterial for improved efficiency and reduced EMF [14]. Yeonje *et al.* also propose a thin hybrid metamaterial slab (HMS) with negative and zero permeability by using a thin printed circuit board (PCB) for high efficiency and low EMF [15]. Jaehyoung *et al.* propose a compact resonant reactive shielding coil topology for reducing EMF in a near-field WPT mobile device application [16]. Xi Lin *et al.* propose approximation formulae to conservatively estimate human exposure to close-range resonant wireless power transfer systems for mobile devices [17]. Andreas *et al.* assess the specific absorption rate (SAR) of a representative wireless power transfer system based on coupled magnetic resonance, and develop novel numerical and experimental approaches to provide a scientifically sound estimate of the human exposure to such systems [18].

Another EMI issue caused by WPT systems for mobile applications is the radiated emissions from common-mode (CM) current flowing in the cables connecting the power transmitter (Tx) and power source. Analysis and modeling of the radiated emissions are provided in [19], but it mistakenly neglects the effects of the coil on the CM EMI. The modeling is not rigorous and only applied to standby mode. This paper is an extension of [19]. It reports analytical modeling of the CM conducted EMI noise from a Qi-compliant WPT system up to 30 MHz for the first time.

This paper is organized as follows. Section 2 describes the schematic diagram of the WPT system and measurement setup of the conducted EMI. Section 3 explains the current path for the CM EMI noise, and then derives the equivalent circuit model and analytical equations for the transfer function. Section 4 validates the model by comparing the predicted CM EMI spectrum with the measurement result. Section 5 discusses the design guidelines for CM EMI issues based on the model. The last section concludes the paper.

2. SCHEMATIC DIAGRAM AND MEASUREMENT SETUP

The WPT system under investigation in this paper is specifically designed for mobile applications and compliant to the Qi standard. The schematic diagram of the WPT system is shown in Figure 1. In the Tx side, the input dc voltage is converted to a square-wave voltage by a full-bridge inverter which is composed of four 30V/30A power MOSFETs. A Pulse Width Modulation (PWM) signal generated by the microcontroller unit (MCU) is used to control the on and off of MOSFETs. The square-wave voltage drives the Tx coil including the Tx matching capacitor to generate current flowing through the coil and time-varying magnetic field perpendicular to the coil. Since the Tx coil and receiver (Rx) coil are coupled, the time-varying magnetic field will also pass through the Rx coil and induce an ac voltage in the Rx coil according to the Faraday's law. In the Rx side, the ac voltage is rectified to dc voltage and then filtered by the smoothing capacitor C_{load}. Usually, C_{load} is sufficiently large to reduce the voltage ripple.

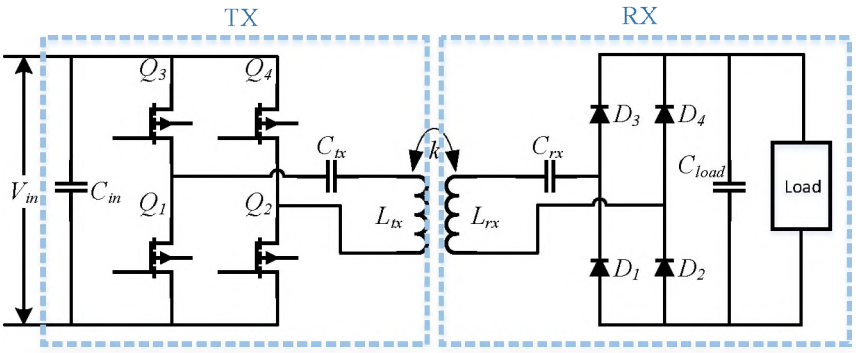

Figure 1. Schematic diagram of the WPT system.

The measurement setup of conducted EMI noise is shown in Figure 2. A sufficiently large metal plate is used as the reference ground. The printed circuit board (PCB) and Tx coil are 2mm high above the reference ground. The Rx is put above the Tx coil. The line impedance stabilization network (LISN) is inserted before the WPT system to measure the conducted EMI noise with L_{LN} = 5 µH, R_{LN} =50 Ohm, C_{LN1} = 1 µF, and C_{LN2} = 0.1 µF. To make the measurement repeatable, the relative position of the Tx coil and Rx coil is fixed, and the output of the battery charger IC in the Rx side is connected to a ceramic resistor.

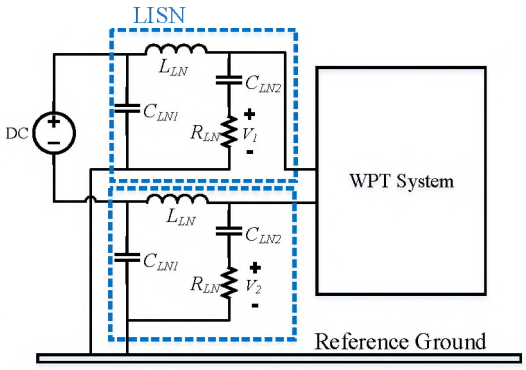

(a)

Figure 2. Measurement setup of conducted EMI. (a) Schematic diagram. (b) Test arrangement.

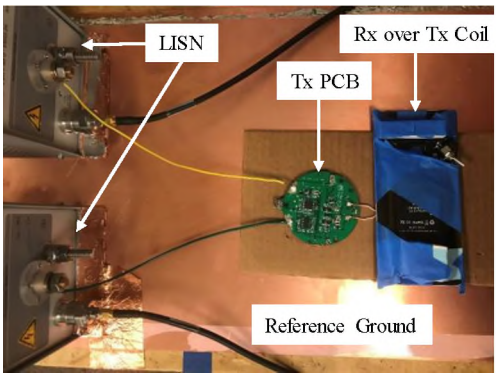

(b)

Figure 2. Measurement setup of conducted EMI. (a) Schematic diagram. (b) Test arrangement, (Cont.).

Suppose V_1 and V_2 are the voltage across the two LISN resistors, the CM conducted EMI noise is defined as

$$V_{cm} = \frac{V_1 + V_2}{2}. \quad (1)$$

3. EMI CURRENT PATH AND EQUIVALENT CIRCUIT MODEL

It is known that the CM EMI noises in power supplies are mainly caused by the rapid switching of MOSFET/IGBT and the parasitic capacitances between drain/collector of MOSFET/IGBT to reference ground [20]-[22]. Similarly, the CM EMI noise in the WPT system is mainly caused by the switching of the MOSFETs in the Tx side. Differently, the parasitic capacitance between the Tx coil and reference ground provides a path for the CM EMI current in addition to the parasitic capacitances between the drain side of MOSFETs and reference ground. The CM EMI current path for one leg of the full-bridge inverter is shown in Figure 3. C_{gs} represents the parasitic capacitance between the drain side of the

low-side power MOSFETs and reference ground. Since the PCB layout areas of the drain side of the low-side power MOSFETs for the two legs of the full-bridge inverter are almost the same, the parasitic capacitances for the two legs are assumed to be the same. C_{gc} represents the total parasitic capacitance between the Tx coil and reference ground. C_{gg} represents the parasitic capacitance between the PCB ground and reference ground. The CM EMI current will go to reference ground through C_{gs} and C_{gc}, and return through the two LISNs to form a relatively large current loop. This current loop will also cause radiated emissions in high frequency.

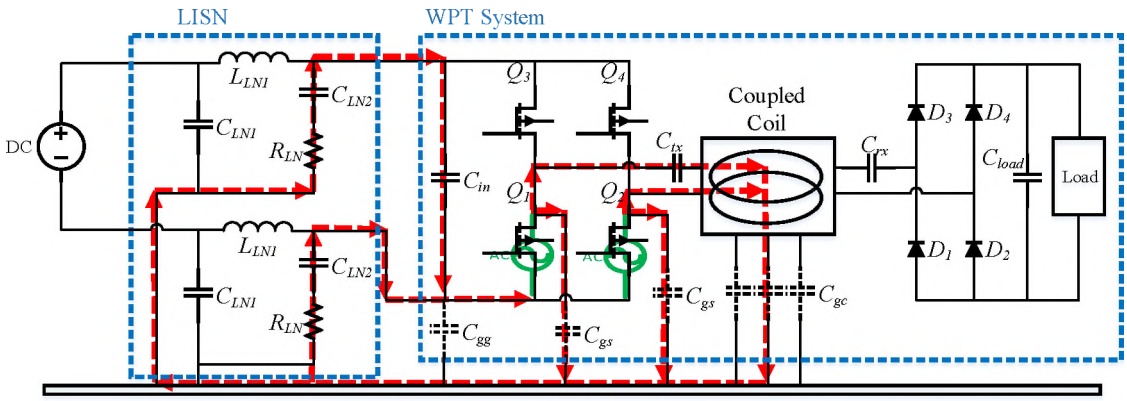

Figure 3. CM EMI current path for one leg of the full-bridge inverter.

3.1. THE IMPEDANCE OF INPUT CAPACITOR CIN AND MATCHING CAPACITOR C_{tx}

The input capacitor C_{in} mainly has two functions. One function is to decrease the power line impedance so that the input voltage fluctuation is reduced. The other function is to filter the generated differential-mode (DM) EMI noise. The impedance of C_{in} is usually small so it can be treated as short circuit. In this specific device under test (DUT), C_{in} is composed of two 22 μF capacitors and two 0.1 μF capacitors.

The Tx side of the WPT system compliant to the Qi standard is typically designed to resonate at around 100 kHz. For this DUT, the Tx coil has an inductance of 4.756 μH, and the Tx matching capacitance is 400 nF, so the resonance frequency can be calculated as

$$Freq_{res} = \frac{1}{2\pi\sqrt{L_{tx}C_{tx}}} = 115.4\,\text{kHz}. \quad (2)$$

In the frequency range of interest for conducted EMI noise which is well above the resonance frequency, the differential impedance of the Tx tank is dominated by L_{tx}, so C_{tx} can also be treated as short circuit.

The impedance of C_{in} and C_{tx} in this DUT is also measured as shown in Figure 4. In the whole frequency range of interest, the impedance is below 1 Ohm, which validates the previous analysis.

3.2. MODELING OF THE DISPLACEMENT CURRENT FLOWING THROUGH PARASITIC CAPACITANCE BETWEEN TX COIL AND REFERENCE GROUND C_{gc}

Modeling of the displacement current flowing through C_{gc} is a major difficulty since the electric potential varies along the coil. To simplify the modeling, two assumptions similar to the modeling of displacement current flowing through the inter-winding capacitance of transformers [23]-[25] are made. The first assumption is that the electric potential varies linearly along the Tx coil. The second assumption is that the parasitic capacitance between the Tx coil and reference ground is evenly distributed. The second assumption holds because the cross-section of litz wire remains unchanged along the coil, and the Tx coil is planar with the coil plane parallel to the reference ground as shown in Figure 5.

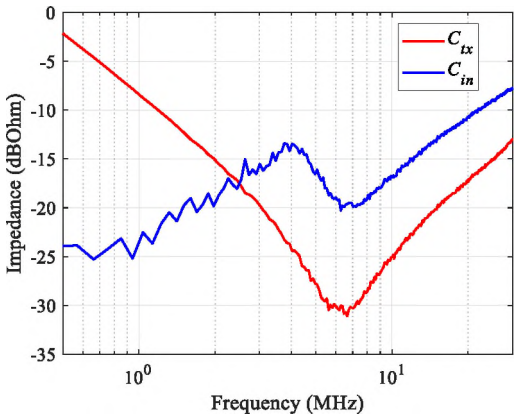

Figure 4. Impedance of C_{in} and C_{tx}.

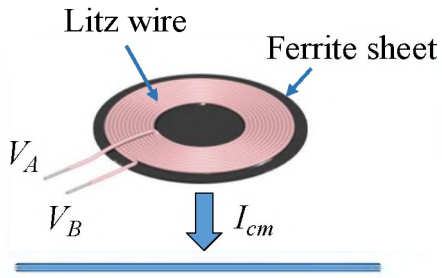

Figure 5. Tx coil and reference ground.

For the Tx coil shown in Figure 5, set the terminal A as the origin and the terminal B as the end, and select any point P from the winding. The electric potential at the two terminals of Tx coil is denoted by V_A and V_B, and the electric potential at point P is denoted by V_P. The total length of the litz wire is denoted by lcoil, and the length from P to A along the winding is denoted by l. The per-unit-length capacitance of the coil at point P is denoted by C_P.

Based on the first assumption, electric potential $V_p(l)$ at point P can be obtained as shown in Figure 6(a). $V_P(l)(0 \leq l \leq l_{coil})$ is given by

$$V_P(l) = V_A + \frac{V_B - V_A}{l_{coil}} l. \tag{3}$$

Based on the second assumption, per-unit-length capacitance $C_P(l)$ at point P can be obtained as shown in Figure 6(b). $C_P(l)(0 \le l \le l_{coil})$ is given by

$$C_P(l) = \frac{C_{gc}}{l_{coil}}. \tag{4}$$

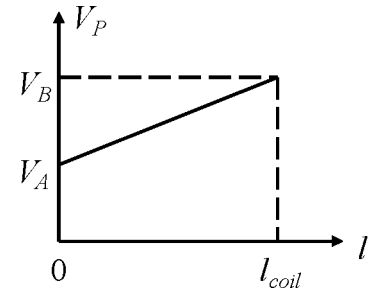

(a)

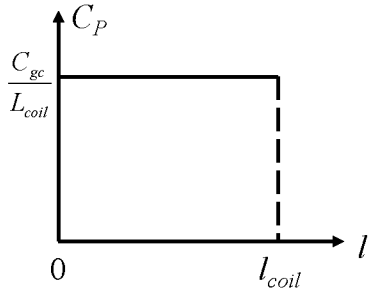

(b)

Figure 6. (a) Electric potential, (b) Per-unit-length capacitance along the coil.

Suppose the electric potential of the reference ground is zero, the displacement current from the Tx coil to reference ground can be calculated as

$$I_{cm}^{coil} = \int_0^{l_{coil}} j2\pi f C_p(l) V_P(l) dl$$

$$= \int_0^{l_{coil}} j2\pi f \frac{C_{gc}}{l_{coil}} (V_A + \frac{V_B - V_A}{l_{coil}} l) dl$$

$$= j2\pi f \frac{C_{gc}}{2} (V_A + V_B), \quad (5)$$

where f is the frequency of interest.

From (5), the displacement current flowing through C_{gc} can be modeled by adding parasitic capacitances of $C_{gc}/2$ between the two terminals of Tx coil and reference ground. This greatly simplifies the modeling.

3.3. MODELING OF THE DISPLACEMENT CURRENT FLOWING THROUGH PARASITIC CAPACITANCE BETWEEN TX COIL AND PCB GROUND C_{pc}

The displacement current flowing through C_{pc} can be modeled in a similar way to 3.2 by adding parasitic capacitances of $C_{pc}/2$ between the two terminals of Tx coil and PCB ground. Since C_{tx} can be treated as short circuit, the two parasitic capacitances are connected in parallel to the low-side MOSFETs of the two legs of the full-bridge inverter. Because the two low-side power MOSFETs can be treated as two independent voltage sources based on the technique developed in [26], the two parasitic capacitances of $C_{pc}/2$ will not change the CM EMI transfer function and they do not need to be included in the equivalent circuit model.

3.4. EQUIVALENT CIRCUIT MODEL

To obtain the equivalent circuit model, the low-side power MOSFETs of the two legs of the full-bridge inverter are substituted by two voltage sources. The voltage sources shall have the same time-domain waveforms as the original voltage across the MOSFETs.

The final equivalent circuit model for the CM EMI noise is shown in Figure 7 by including the voltage sources and all linear circuit elements which affect the CM EMI noise.

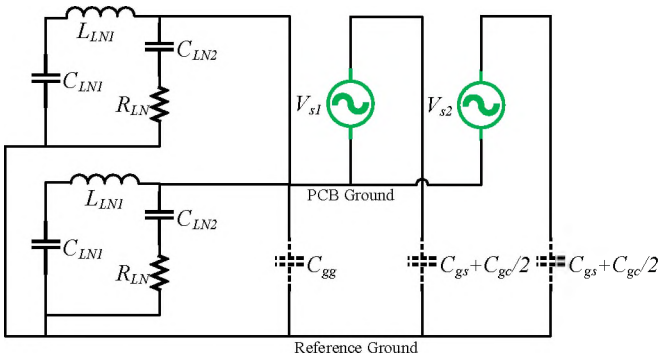

Figure 7. Equivalent circuit model for the CM EMI noise.

Since the two voltage sources are independent, the CM EMI noise generated from one voltage source can be derived by replacing the other voltage source with short circuit.

The CM EMI noise V_{cm1} generated by voltage source V_{s1} can be derived as

$$V_{cm1} = V_{gg} k_1 = V_{s1} \frac{Z_{gg}}{Z_{gg} + \dfrac{1}{j2\pi f (C_{gs} + C_{gc}/2)}} k_1, \tag{6}$$

where V_{gg} is the voltage difference between PCB ground and reference ground, Z_{gg} is the impedance between PCB ground and reference ground, and k_1 is given by

$$k_1 = \frac{R_{LN}}{R_{LN} + \dfrac{1}{j2\pi f C_{LN2}}}. \tag{7}$$

Z_{gg} can be calculated by

$$Z_{gg} = \frac{1}{j2\pi f (C_{gg} + C_{gs} + C_{gc}/2) + G_{LN}}, \tag{8}$$

where G_{LN} is given by

$$G_{LN} = \frac{2}{j2\pi fL_{LN1} + \frac{1}{j2\pi fC_{LN1}}} + \frac{2}{R_{LN} + \frac{1}{j2\pi fC_{LN2}}}. \quad (9)$$

Substituting (8) into (6) and simplifying the equation yields

$$V_{cm1} = V_{s1} \frac{j2\pi f(C_{gs} + C_{gc}/2)}{j2\pi f(C_{gg} + 2C_{gs} + C_{gc}) + G_{LN}} k_1. \quad (10)$$

Similarly, the CM EMI noise V_{cm2} generated by voltage source V_{s2} can be derived as

$$V_{cm2} = V_{s2} \frac{j2\pi f(C_{gs} + C_{gc}/2)}{j2\pi f(C_{gg} + 2C_{gs} + C_{gc}) + G_{LN}} k_1. \quad (11)$$

Based on the superposition theorem, the total CM EMI noise V_{cm} is the sum of V_{cm1} and V_{cm2}. Therefore, the transfer function H_{cm} relating the total CM EMI noise V_{cm} to noise source $V_{s1} + V_{s2}$ can be derived as

$$H_{cm} = \frac{V_{cm}}{V_{s1} + V_{s2}} = \frac{j2\pi f(C_{gs} + C_{gc}/2)}{j2\pi f(C_{gg} + 2C_{gs} + C_{gc}) + G_{LN}} k_1, \quad (12)$$

where k_1 and G_{LN} are only related to the LISN circuits.

4. VALIDATION OF THE MODEL

4.1. THE SPECTRUM OF NOISE SOURCE

The time-domain waveforms of the two voltage sources V_{s1} and V_{s2} are directly measured using two active probes and oscilloscope. The delay of the two active probes must be the same to obtain the correct time-domain waveform of $V_{s1}+V_{s2}$. This can be checked by measuring the same signal using the two active probes firstly. It is expected that the measured time-domain waveforms should be the same without any timing

difference. The time-domain waveform of $V_{s1}+V_{s2}$ is converted to the frequency domain via FFT to get its spectrum as shown in Figure 8.

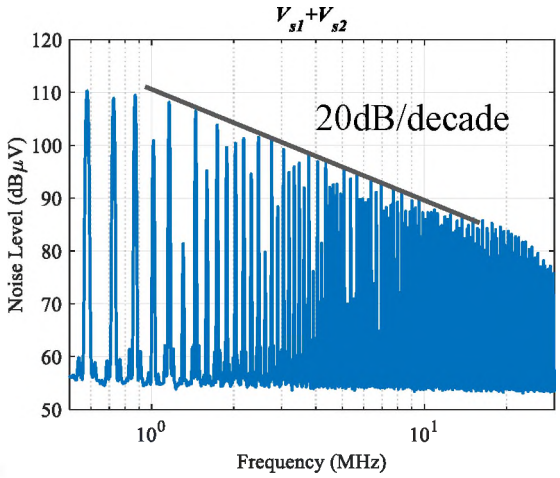

Figure 8. Spectrum of noise source voltage.

4.2. VALUE OF PARASITIC CAPACITANCES

The values of C_{gs} and C_{gg} are mainly decided by the layout area and the distance between the PCB and reference ground. Their value can be estimated by full-wave simulation using ANSYS Q3D Extractor [27] or EMCoS Low Frequency Electric Field Solver [28] since the 3D model can be easily built from PCB layout files. The simulation model is shown in Figure 9. From the simulation result, C_{gs} = 0.07 pF, C_{gg} = 14.6 pF.

The value of C_{gc} is mainly decided by the Tx coil size and the distance between coil and reference ground. Since it is not easy to build a 3D model of the coil, and the ferrite sheet underneath the coil will also affect the capacitance value, C_{gc} is measured. The measurement setup is shown in Figure 10. The two terminals of the Tx coil are shorted together. The outer shield of the coaxial cable is connected to the reference ground and the

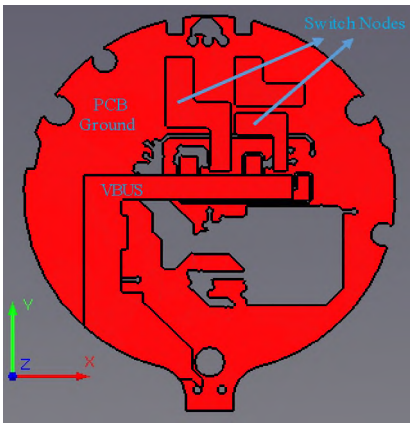

Figure 9. Simulation model for C_{gs} and C_{gg}.

inner pin of the coaxial cable is connected to the coil terminal. A vector network analyzer (VNA) is used to measure the S_{11} at the end of coaxial cable.

The impedance between the coil terminal and reference ground Z_c can be calculated from S_{11} by

$$Z_c = 50\,\frac{1 + S_{11}}{1 - S_{11}}. \tag{13}$$

The impedance versus frequency at different DUT heights is shown in Figure 11. The impedance follows a 20 dB decrease per decade, which shows that it is in the capacitive region. There are some noises at low frequency because Z_c is very sensitive to S_{11} when S_{11} is close to 1. The noise in the S_{11} measurement will be "amplified" in Z_c.

From measured impedance @ 10MHz where the noise is small, the capacitance can be calculated by

$$C_{gc} = \frac{1}{|Z_c @ 10MHz| * 2\pi * 10MHz}. \tag{14}$$

Based on (13), when the DUT height is around 2mm, C_{gc} = 11.5 pF; when the height DUT is around 4mm, C_{gc} = 9.8 pF; when the DUT height is around 6mm, C_{gc} = 8.2 pF.

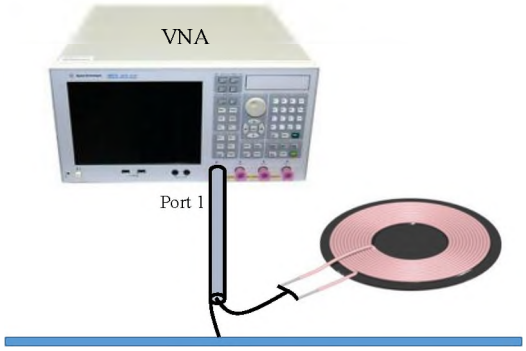

Figure 10. Measurement setup for C_{gc}.

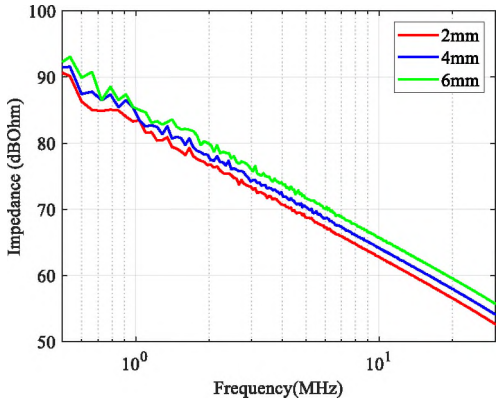

Figure 11. Impedance between the coil terminal and reference ground.

4.3. COMPARISON OF PREDICTED AND MEASURED CM EMI NOISE

After the spectrum of V_{s1}+V_{s2} is obtained and H_{cm} is calculated by (12), the CM EMI noise can be predicted by

$$V_{cm} = H_{cm}(V_{s1} + V_{s2}). \tag{15}$$

When the DUT height is 2mm, the calculated transfer function using (12) is shown in Figure 12, and the predicted CM EMI noise is compared with the measurement result as shown in Figure 13. The prediction matches well with measurement.

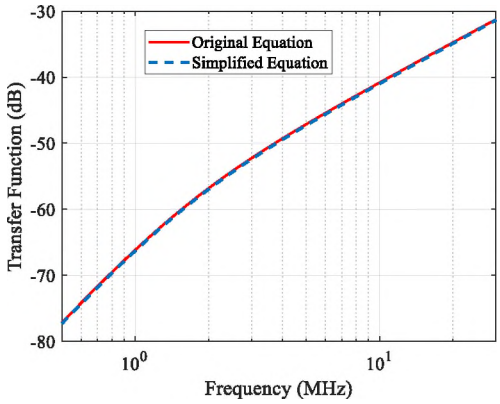

Figure 12. Transfer function when DUT height is 2mm.

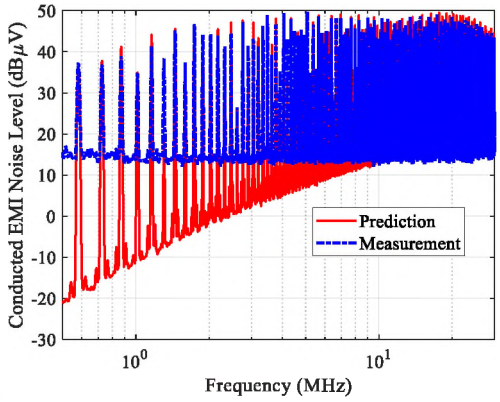

Figure 13. Comparison of predicted and measured CM EMI noise.

5. GUIDELINES FOR CM EMI DESIGN

5.1. REDUCE THE SPECTRUM OF NOISE SOURCE

The CM EMI noise will be reduced if the spectrum of the noise source is reduced. The time-domain waveform of V_{s1}+V_{s2} can be approximated as a periodic trapezoidal waveform with the same rise time and fall time. Given the voltage amplitude A, the period

T, the pulse width τ, and the rise time τ_r, the spectrum envelop of the waveform can be calculated analytically as

$$envelop = \frac{2A\tau}{T}\left|\frac{\sin(\pi\tau f)}{\pi\tau f}\right|\left|\frac{\sin(\pi\tau_r f)}{\pi\tau_r f}\right|. \tag{16}$$

From (14), the direct way to reduce the spectrum of the noise source is to increase T and reduce A, indicating reducing the switching frequency and DC bus voltage. Increasing τ_r, indicating slowing down transition time, will help in the higher frequency range. This can be realized by adding Y capacitors in parallel to the low-side MOSFETs of the two legs of full-bridge inverter. But increasing τ_r also means increased switching loss, so there is a compromise between the switching loss and EMI.

5.2. REDUCE THE TRANSFER FUNCTION

The CM EMI noise will be reduced if the transfer function is reduced. The most straightforward way to reduce the transfer function is to insert CM chokes in the CM EMI current path. The CM choke is usually inserted before C_{in}.

The parasitic capacitances will also affect the transfer function. The effects of the parasitic capacitances on the transfer function can be analyzed based on (12).

From the measured and simulated value of parasitic capacitances,

$$C_{gs} \ll C_{gc}/2, \tag{17}$$

so C_{gs} can be neglected. Below 30MHz, based on the LISN circuits and value of parasitic capacitances,

$$j2\pi f(C_{gg} + 2C_{gs} + C_{gc}) \ll G_{LN}. \tag{18}$$

Therefore, (12) can be simplified as

$$H_{cm} = \frac{j\pi f C_{gc}}{G_{LN}} k_1. \tag{19}$$

When the DUT height is 2mm, the calculated transfer function using (19) is also shown in Figure 12. The calculated transfer function using the original equation and the simplified equation is the same, which validates the simplification.

Based on (19), when the DUT height is changed from 2mm to 4mm, the reduction in CM EMI can be calculated as

$$20\log_{10}\left(\frac{\left|H_{cm}\right|_{DUT\,height=4mm}}{\left|H_{cm}\right|_{DUT\,height=2mm}}\right) = 20\log_{10}\left(\frac{C_{gc}\big|_{DUT\,height=4mm}}{C_{gc}\big|_{DUT\,height=2mm}}\right) = -1.39dB. \tag{20}$$

When the DUT height is changed from 4mm to 6mm, the reduction in CM EMI can be calculated as

$$20\log_{10}\left(\frac{\left|H_{cm}\right|_{DUT\,height=6mm}}{\left|H_{cm}\right|_{DUT\,height=4mm}}\right) = 20\log_{10}\left(\frac{C_{gc}\big|_{DUT\,height=6mm}}{C_{gc}\big|_{DUT\,height=4mm}}\right) = -1.55dB. \tag{21}$$

The CM EMI noises when the DUT height is 4mm and 6mm are also measured as shown in Figure 14 to compare with the measurement result with a DUT height of 2mm. The reduction with the increase of DUT height is close to our prediction and this verifies (19).

Based on (19), the only parasitic capacitance which affects the transfer function below 30MHz is C_{gc}. To reduce the transfer function, C_{gc} should be reduced. Since C_{gc} is mainly decided by the coil size, the size of the coil should be kept as small as possible. This also indicates that C_{gc} can be used as a factor to evaluate the EMI performance of coil design. Another method to reduce C_{gc} is to shield the electric fields between the coil and reference ground using conductive metal, but this will more or less change the original

magnetic field distribution and introduce additional loss due to induced eddy current in the metal.

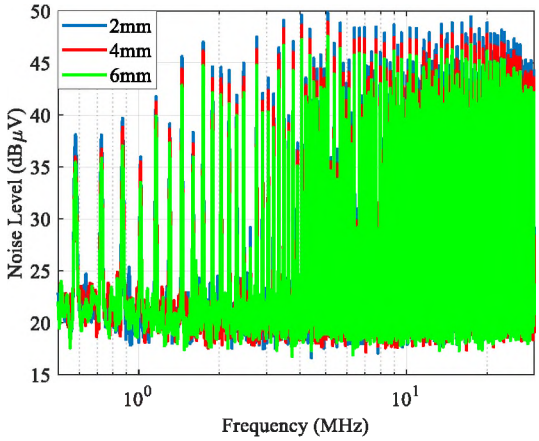

Figure 14. Measured CM EMI noise at different DUT heights.

6. CONCLUSIONS

This paper analyzes and models the conducted CM EMI noise from a WPT system for mobile applications up to 30MHz. By assuming that the electric potential varies linearly and C_{gc} is evenly distributed along the Tx coil, the displacement current flowing through C_{gc} can be modeled by adding parasitic capacitance of $C_{gc}/2$ between the two terminals of Tx coil and reference ground. The noise source of the CM EMI is $V_{s1}+V_{s2}$ of which the time-domain waveform is measured and the spectrum is obtained via FFT. The frequency-domain transfer function H_{cm} is calculated using the derived analytical equation. The CM EMI spectrum is predicted by multiplying the spectrum of noise source by transfer function and the prediction matches well with measurement. By further simplifying the equation of

transfer function, it can be concluded that the transfer function is only affected by C_{gc} and is proportional to C_{gc}.

REFERENCES

[1] N. Shinohara, "Power without wires," *IEEE Microw. Mag.*, vol. 12, no. 7, pp. S64–S73, Dec. 2011.

[2] J. Shin et al., "Design and implementation of shaped magnetic-resonance-based wireless power transfer system for roadway-powered moving electric vehicles," *IEEE Trans. Ind. Electron.*, vol. 61, no. 3, pp. 1179–1192, Mar. 2013.

[3] C. C. Mi, G. Buja, S. Y. Choi, and C. T. Rim, "Modern advances in wireless power transfer systems for roadway powered electric vehicles," *IEEE Trans. Ind. Electron.*, vol. 63, no. 10, pp. 6533–6545, Oct. 2016.

[4] S. Li and C. C. Mi, "Wireless power transfer for electric vehicle applications," *IEEE J. Emerg. Sel. Topics Power Electron.*, vol. 3, no. 1, pp. 4–17, Mar. 2015.

[5] X. Lu, P. Wang, D. Niyato, D. I. Kim, and Z. Han, "Wireless charging technologies: Fundamentals, standards, and network applications," *IEEE Commun. Surv. Tut.*, vol. 18, no. 2, pp. 1413–1452, Apr.–Jun. 2016.

[6] D. Ahn and S. Hong, "Wireless power transmission with self-regulated output voltage for biomedical implant," *IEEE Trans. Ind. Electron.*, vol. 61, no. 5, pp. 2225–2235, May 2014.

[7] D. Van Wageningen and T. Staring, "The QI wireless power standard," in *Proc. 14th Int. IEEE Power Electron. Motion Control Conf.*, 2010, pp. S15 25.

[8] R. Tseng, B. v. Novak, S. Shevde, and K. Grajski, "Introduction to the alliance for wireless power loosely-coupled wireless power transfer system specification version 1.0," in *Proc. IEEE Wireless Power Transfer*, May 15–16, 2013, pp. 79–83.

[9] H. Kim et al., "Coil design and measurements of automotive magnetic resonant wireless charging system for high-efficiency and low magnetic field leakage," *IEEE Trans. Microw. Theory Techn.*, vol. 64, no. 2, pp. 383–400, Feb. 2016.

[10] C. Song et al., "Low EMF and EMI design of a tightly coupled handheld resonant magnetic field (HH-RMF) charger for automotive battery charging," *IEEE Trans. Electromagn. Compat.*, vol. 58, no. 4, pp. 1194–1206, Aug. 2016.

[11] M. Kim, H. Kim, D. Kim, H.-H. Park, S. Ahn, and Y. Jeong, "A three-phase wireless-power-transfer system for online electric vehicles with reduction of leakage magnetic fields," *IEEE Trans. Microw. Theory Techn.*, vol. 63, no. 11, pp. 3806–3813, Nov. 2015.

[12] S. Park, "Evaluation of electromagnetic exposure during 85 kHz wireless power transfer for electric vehicles," *IEEE Trans. Magn.*, vol. 54, no. 1, Jan. 2018, Art. no. 5100208

[13] S. Kong et al., "An investigation of electromagnetic radiated emission and interference from multi-coil wireless power transfer systems using resonant magnetic field coupling," *IEEE Trans. Microw. Theory Techn.*, vol. 63, no. 3, pp. 833–845, Mar. 2015.

[14] Y. Cho et al., "Thin PCB-type metamaterials for improved efficiency and reduced EMF Leakage in wireless power transfer systems," *IEEE Trans. Microw. Theory Technol.*, vol. 64, no. 2, pp. 353–364, Feb. 2016

[15] Y. Cho et al., "Thin hybrid metamaterial slab with negative and zero permeability for high efficiency and low electromagnetic field in wireless power transfer systems," *IEEE Trans. Electromagn. Compat.*, vol. 60, no. 4, pp. 1001–1009, Aug. 2018.

[16] J. Park et al., "A resonant reactive shielding for planar wireless power transfer system in smartphone application," *IEEE Trans. Electromagn. Compat.*, vol. 59, no. 2, pp. 695–703, Apr. 2017.

[17] X. L. Chen, A. E. Umenei, N. Chavannes, V. De Santis, J. Mosig, and N. Kuster, "Human exposure to close-range wireless power transfer systems as a function of design parameters," *IEEE Trans. Electromagn.Compat.*, vol. 56, no. 5, pp. 1027–1034, Oct. 2014.

[18] A. Christ, M. G. Douglas, J. M. Roman, E. B. Cooper, A. P. Sample, B. H. Waters, J. R. Smith, and N. Kuster, "Evaluation of wireless resonant power transfer systems with human electromagnetic exposure limits," *IEEE Trans. Electromagn. Compat.*, vol. 55, no. 2, pp. 265–274, Apr. 2013.

[19] C. Wu, H. Kim, A. Huang, J. Fan, S. Pan, and T. Li, "An investigation of electromagnetic radiated emissions from wireless charging system for mobile device using Qi standard," in *Proc. IEEE Symp. Electromagn. Compat. Signal Integrity Power Integrity*, Long Beach, CA, USA, 2018, pp. 483–488.

[20] X. Pei, K. Zhang, Y. Kang, and J. Chen, "Prediction of common mode conducted EMI in single phase PWM inverter," in *Proc. IEEE Power Electron. Spec. Conf.*, Aachen, Germany, Jun. 20–25, 2004, pp. 3060–3065.

[21] C. Wu et al., "Analysis and Modeling of Conducted EMI from an AC–DC Power Supply in LED TV up to 1 MHz," *IEEE Trans. Electromagn. Compat.*, vol. 61, no. 6, pp. 2050–2059, Dec. 2019.

[22] H. Zhang, S. Wang, Y. Li, Q. Wang, and D. Fu, "Two-capacitor transformer winding capacitance models for common-mode EMI noise analysis in isolated DC–DC converters," *IEEE Trans. Power Electron.*, vol. 32, no. 11, pp. 8458–8469, Nov. 2017.

[23] D. Fu, S. Wang, P. Kong, F. C. Lee, and D. Huang, "Novel techniques to suppress the common-mode EMI noise caused by transformer parasitic capacitances in DC-DC converters," *IEEE Trans. Ind. Electron.*, vol. 60, no. 11, pp. 4968–4977, Nov. 2013.

[24] L. H. Xie, X. B. Ruan, and Z. H. Ye, "Equivalent noise source: An effective method for analyzing common-mode noise in isolated power converters," *IEEE Trans. Ind. Electron.*, vol. 63, no. 5, pp. 2913–2924, May 2016.

[25] Y. B. Chu and S. Wang, "A generalized common-mode current cancelation approach for power converters," *IEEE Trans. Ind. Electron.*, vol. 62, no. 7, pp. 4130–4140, Jul. 2015.

[26] S. Wang, P. Kong, and F. C. Lee, "Common mode noise reduction for boost converters using general balance technique," *IEEE Trans. Power Electron.*, vol. 22, no. 4, pp. 1410–1416, Jul. 2007.

[27] ANSYS Q3D Extractor. 2019. [Online]. Available: https://www.ansys.com/products/electronics/ansys-q3d-extractor

[28] EMCos Studio. 2019. [Online]. Available: https://www.emcos.com/

SECTION

2. CONCLUSIONS

The first paper proposes an improved method to extract dipoles from magnitude-only electromagnetic-field data. Two contributions are made to the current study. The first contribution is that it improves the iteration approach of the back-and-forth iteration algorithm in and enables the algorithm to work for electromagnetic-field data on a single scanning surface and arbitrarily-shaped scanning surfaces. The second contribution is that it combines the genetic algorithm with the back-and-forth iteration algorithm, which makes the algorithm automatic without predetermination of the type and location of dipoles. It also minimizes the number of required dipoles because of the gradual increment of dipole number. But bringing in the genetic algorithm also means increased computation time, especially when the number of extracted dipoles is large. Therefore, the algorithm is suitable for EMI applications, where the noise source can be modeled using a few dipoles.

In the second paper, the conducted EMI below 1 MHz from the ac to dc power supply in a LED TV is analyzed and modeled. STFFT is used to analyze the noise source voltage and conducted EMI. The drain-to-source voltage of power MOSFET in the PFC converter is identified as the dominant noise source of both DM and CM EMI below 1 MHz. The EMI current path is different during different periods of the cycle. During most time of the cycle, two diodes of the bridge rectifier are forward biased. When the ac voltage is crossing zero, at most one diode of the bridge rectifier is forward biased, the DM EMI will be much smaller. This short time can be neglected when we consider the max hold

spectrum. When the bridge rectifier is forward biased, the bridge rectifier can be treated as short circuit, and the current paths of DM and CM EMI are explained and modeled by a linear equivalent circuit model. Three parasitic capacitances need to be considered to model the CM EMI in this DUT. From the circuit model, the transfer function relating DM and CM EMI spectrum to noise source voltage spectrum are obtained. The conducted EMI is predicted by multiplying the measured noise source voltage by the transfer function. The prediction matches well with measurement. The effects of parasitic capacitances C_{p1}, C_{p2}, and C_{p3} on CM EMI are analyzed by simulation and then validated by measurement. The analysis can help with EMI design to reduce the CM EMI.

The last paper analyzes and models the conducted CM EMI noise from a WPT system for mobile applications up to 30MHz. By assuming that the electric potential varies linearly and C_{gc} is evenly distributed along the Tx coil, the displacement current flowing through C_{gc} can be modeled by adding parasitic capacitance of $C_{gc}/2$ between the two terminals of Tx coil and reference ground. The noise source of the CM EMI is $V_{s1}+V_{s2}$ of which the time-domain waveform is measured and the spectrum is obtained via FFT. The frequency-domain transfer function H_{cm} is calculated using the derived analytical equation. The CM EMI spectrum is predicted by multiplying the spectrum of noise source by transfer function and the prediction matches well with measurement. By further simplifying the equation of transfer function, it can be concluded that the transfer function is only affected by C_{gc} and is proportional to C_{gc}.

VITA

Chunyu Wu was born in Chibi, Hubei, China. He received the B.S. degree in Electronics and Information Engineering from Huazhong University of Science and Technology, Wuhan, China, in 2014. He joined the Electromagnetic Compatibility (EMC) Laboratory at Missouri University of Science and Technology, Rolla, in 2014 and received a Master of Science in Electrical Engineering in May 2017. He received a Doctor of Philosophy in Electrical Engineering in December 2020 from Missouri University of Science and Technology. His research interests included EMC and signal integrity (SI).